Photochemical degradation of iron(III)-citrate/citric acid aerosol quantified with the combination of three complementary experimental techniques and a kinetic process model

Jing Dou[1], Peter A. Alpert[2], Pablo Corral Arroyo[2*], Beiping Luo[1], Frederic Schneider[2], Jacinta Xto[3], Thomas Huthwelker[3], Camelia N. Borca[3], Katja D. Henzler[3], Jörg Raabe[4], Benjamin Watts[4], Hartmut Herrmann[5], Thomas Peter[1], Markus Ammann[2], and Ulrich K. Krieger[1]

[1]Institute for Atmospheric and Climate Science, ETH Zürich, 8092 Zürich, Switzerland
[2]Laboratory of Environmental Chemistry, Paul Scherrer Institute, 5232 Villigen, Switzerland
[3]Laboratory for Synchrotron Radiation and Femtochemistry, Paul Scherrer Institute, 5232 Villigen, Switzerland
[4]Laboratory for Synchrotron Radiation-Condensed Matter, Paul Scherrer Institute, 5232 Villigen, Switzerland
[5]Atmospheric Chemistry Department (ACD), Leibniz-Institute for Tropospheric Research (TROPOS), 04318 Leipzig, Germany
[*]now at: Department of Chemistry and Applied Biosciences, ETH Zürich, 8093 Zürich, Switzerland

Correspondence: Jing Dou (jing.dou@env.ethz.ch) and Ulrich K.Krieger (ulrich.krieger@env.ethz.ch)

Abstract.

Iron(III) carboxylate photochemistry plays an important role in aerosol aging, especially in the lower troposphere. These complexes can absorb light over a broad wavelength range, inducing the reduction of iron(III) and the oxidation of carboxylate ligands. In the presence of O_2, ensuing radical chemistry leads to further decarboxylation, and the production of $\cdot OH$, HO_2,

5   peroxides, and oxygenated volatile organic compounds, contributing to particle mass loss. The $\cdot OH$, HO_2, and peroxides in turn re-oxidize iron(II) back to iron(III), closing a photocatalytic cycle. This cycle is repeated resulting in continual mass loss due to the release of CO_2 and other volatile compounds. In a cold and/or dry atmosphere, organic aerosol particles tend to attain highly viscous states. While the impact of reduced mobility of aerosol constituents on dark chemical reactions has received substantial attention, studies on the effect of high viscosity on photochemical processes are scarce. Here, we choose

10   iron(III)-citrate ($Fe^{III}(Cit)$) as a model light absorbing iron carboxylate complex that induces citric acid (CA) degradation to investigate how transport limitations influence photochemical processes. Three complementary experimental approaches were used to investigate kinetic transport limitations. The mass loss of single, levitated particles was measured with an electrodynamic balance, the oxidation state of deposited particles was measured with X-ray spectromicroscopy, and HO_2 radical production and release into the gas phase was observed in coated wall flow tube experiments. To quantitatively compare these

15   experiments and determine important physical and chemical parameters, a numerical multi-layered photochemical reaction and diffusion (PRAD) model that treats chemical reactions and transport of various species was developed. We observed significant photochemical degradation, with up to 80 % mass loss within 24 hours of light exposure. Interestingly, we also observed that mass loss always accelerated during irradiation, resulting in an increase of the mass loss rate by about a factor of 10. When we increased relative humidity, the observed particle mass loss rate also increased. This is consistent with strong kinetic transport

20   limitations for highly viscous particles. The PRAD model was tuned to reproduce all experimental results and captured the es-

sential chemistry and transport during irradiation. In particular, the photolysis rate of Fe^{III}, the re-oxidation rate of Fe^{II}, HO_2 production, and the diffusivity of O_2 in aqueous $Fe^{III}(Cit)/CA$ system as function of relative humidity and $Fe^{III}(Cit)/CA$ molar ratio could be constrained. Photochemical degradation under atmospheric conditions predicted by the PRAD model shows that release of CO_2 and re-partitioning of organic compounds to the gas phase may be very significant to accurately predict

25   organic aerosol aging processes.

1   Introduction

Photochemistry in the atmosphere (either in the gas phase or in the particle phase) plays an important role in aerosol aging processes. Photochemically produced free radicals in the gas phase (mainly $\cdot OH$) can be taken up by aerosol particles, inducing multi-phase chemistry. However, uptake is limited by the collision rate and condensed phase molecular transport when

30   diffusion coefficients are sufficiently low, which restricts chemical reactions to the near-surface region of the particle. In contrast, photochemically generated radicals in aerosol particles would be present throughout their bulk due to light penetrating their whole volume. Direct photochemical reaction induced radical production occurs when the energy of light quanta is high enough (mostly the UV part of the solar spectrum) to cause bond cleavage or rearrangement in a molecule. In the lower troposphere where UV light intensity is low, indirect photochemistry initiated by visible radiation may become significant. Important

35   indirect photochemical processes are transition metal complex photochemistry and photosensitized processes (Corral Arroyo et al., 2018; George et al., 2015). This work focuses on iron carboxylate catalyzed photochemistry due to its abundance and reactivity in the atmosphere.

Iron is the most abundant transition metal in the earth's crust. Wind erosion is the main source of iron in the atmosphere, but anthropogenic activities such as industrial processes, traffic and combustion processes can also potentially release iron in

40   particulate form (Deguillaume et al., 2005). Depending on parameters such as temperature, pH value, ionic strength and concentration of involved substances, iron can combine with inorganic or organic ligands to form complexes (Deguillaume et al., 2005; Faust and Hoigné, 1990; Kieber et al., 2005). Iron can be found complexed with low molecular weight inorganic species such as the hydroxide anion (OH^-), sulfate (SO_4^{2-}) and sulfite (SO_3^{2-}) (Brandt and van Eldik, 1995; Hofmann et al., 1991; Weschler et al., 1986). In turn, organic compounds are a major component in atmospheric aerosol particles and have received

45   more and more attention as potential ligands for iron(III) complexation. For instance, humic like substances derived from water soluble organic compounds, have been reported to be strong chelating ligands with iron(III) (Dou et al., 2015; Kieber et al., 2003; Okochi and Brimblecombe, 2002; Willey et al., 2000). Oxalate and other carboxylates have been identified to be important ligands for iron(III) because they are available in sufficient amounts (Chebbi and Carlier, 1996; Kahnt et al., 2014; Kawamura et al., 1985), and the carboxylate groups are acidic enough to dissociate and chelate with iron(III) at atmospheric

50   pH values (Okochi and Brimblecombe, 2002).

In atmospheric aqueous phases, iron normally exists in oxidation states (II) and (III), and they can convert into each other via redox cycling. The ratio between iron(II) and iron(III) in aerosol particles is quite variable, which depends on several factors such as the presence of light, oxidizing compounds, and ligands. For example, iron(III) carboxylate complexes

$[Fe^{III}(OOC-R)]^{2+}$ are well-known photoactive compounds (Wang et al., 2012; Weller et al., 2013, 2014). They can easily
get excited by light in the UV-VIS range, inducing ligand-to-metal charge transfer (LMCT) (Cieśla et al., 2004), which is an
inner sphere electron transfer (i.e., the electron transfer occurs via a covalently bound bridging ligand) from the carboxylate
group to the iron. Investigations using time resolved transient spectroscopy reported the formation of long lived radical com-
plexes, $[Fe^{II}(\cdot OOC-R)]^{2+}$, with lifetimes of the order of a millisecond, followed by the dissociation to the organic radical
$R-COO\cdot$ and an Fe^{II} aquacomplex (Feng et al., 2007; Glebov et al., 2011; Pozdnyakov et al., 2009; Zhang et al., 2009):

$$[Fe^{III}(OOC-R)]^{2+} + h\nu \rightarrow [Fe^{III}(OOC-R)]^{2+*} \tag{R1}$$

$$[Fe^{III}(OOC-R)]^{2+*} \rightarrow [Fe^{II}(\cdot OOC-R)]^{2+} \tag{R2}$$

$$[Fe^{II}(\cdot OOC-R)]^{2+} \rightarrow Fe^{2+} + R-COO\cdot \tag{R3}$$

$R-COO\cdot$ will decarboxylate almost instantaneously ($k_{R4} \approx 10^9 - 10^{12}\,s^{-1}$) (Abel et al., 2003; Bockman et al., 1997; Hilborn
and Pincock, 1991):

$$R-COO\cdot \rightarrow R\cdot + CO_2 \tag{R4}$$

The alkyl radical $R\cdot$ will react rapidly with dissolved O_2, producing a peroxy radical with $k_{R5} \approx 2 \times 10^9\,M^{-1}\,s^{-1}$ (von Sonntag
and Schuchmann, 1991):

$$R\cdot + O_2 \rightarrow RO_2^\cdot \tag{R5}$$

Subsequent reactions of $R\cdot$ and $RO_2^\cdot$ are specific depending on the type of ligand and its substitution.

In this work we investigated iron(III)-citrate ($[Fe^{III}(OOCCH_2)_3C(OH)]$, in short $Fe^{III}(Cit)$), as a model species to better
understand iron carboxylate photochemistry in atmospheric aerosol particles. $Fe^{III}(Cit)$ photochemistry is well established in
both solution (Abida et al., 2012; Faust and Zepp, 1993; Pozdnyakov et al., 2012) and solid states (Abrahamson et al., 1994).
Citric acid (CA) is an established proxy for oxygenated atmospheric organic matter, with its thermodynamic properties, water
diffusivity and viscosity being well studied (Lienhard et al., 2012, 2014; Song et al., 2016). As schematically described in
Fig. 1, $Fe^{III}(Cit)$ absorbs light up to 500 nm, inducing LMCT, followed by immediate decarboxylation of the central carboxyl
group, since the hydroxyl group adjacent to a carboxyl group facilitates decarboxylation (Weller et al., 2013). In the presence
of O_2, oxidants such as $HO_2^\cdot$ and H_2O_2 will be produced, which can oxidize Fe^{II} back to Fe^{III} via Fenton reactions (Fenton,
1894), with additional production of oxidants. Fe^{III} then combines with another citric acid in this aqueous system, closing the
photocatalytic cycle, in which iron acts as a catalyst for CA degradation. In addition, the generation of reactive oxygen species
(ROS) and peroxy radicals leads to further decarboxylation and more production of oxygenated volatile organic compounds
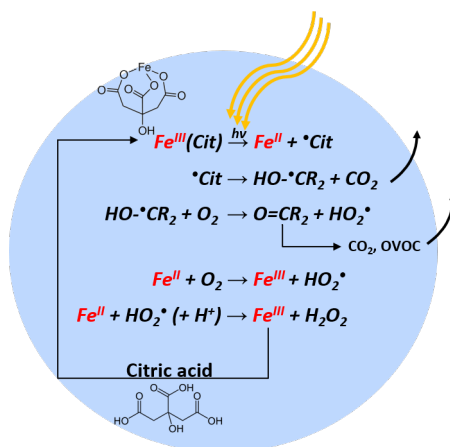
Figure 1. Photocatalytic cycle of Fe^{III}(Cit) complex in an aqueous particle containing citric acid, with explicit charge balance given in Table 2. R corresponds to the carboxylate side chain $-CH_2COO^-$.

(OVOCs) (e.g., acetone) (Pozdnyakov et al., 2008; Wang et al., 2012). Therefore, this photodegradation process is potentially an important sink of carboxylate groups in the troposphere.

85   We expect that continuing chemistry subsequent to initial photochemical reaction steps in the aerosol phase will be significantly altered by diffusion limitations when Fe^{III}(Cit) particles mixed with CA attain a high viscosity. As viscosity increases, molecular diffusion coefficients tend to decrease (Koop et al., 2011) and therefore, photochemical cycling will also be slow. Increasing water content is expected when RH increases and will effectively plasticize particles (Koop et al., 2011) leading to a more well mixed conditions and faster photochemical cycling when compared with lower RH. However, these effects have

90   been investigated in dark systems but not in photochemical systems (Berkemeier et al., 2016; Shiraiwa et al., 2011; Shiraiwa and Seinfeld, 2012; Steimer et al., 2015a). In order to better understand this system and how it reacts to RH, we used a triad of photochemical experiments including electrodynamic balance (EDB), scanning transmission X-ray microscopy coupled with near edge absorption fine structure (STXM/NEXAFS) spectroscopy, and a coated wall flow tube (CWFT) to investigate how particle size, mass, and indicators of chemical composition change during photochemical processes. In this work we mostly

95   focus on the humidity dependence of this photochemical degradation, while Alpert et al. (2020) focus on the impacts on ROS species and the fate of free radicals during this photochemical degradation.

To perform quantitative comparison of these experiments and determination of relevant properties, a numerical multi-layered photochemical reaction and diffusion (PRAD) model that treats chemical reactions and transport of various species was developed. The PRAD model allows to simulate photochemical aging processes under atmospheric conditions. In the following we

100   briefly discuss our experimental approaches in Sect. 2, and include a detailed explanation of the PRAD model in Subsect. 2.4. A comparison between experimental results and the PRAD model is presented in Sect. 3. Finally, we discuss the impact and atmospheric importance of kinetic limitations to photochemical degradation in Sect. 4.

2 Methods

2.1 Bulk property measurements by EDB

105 We used an electrodynamic balance (EDB) to measure the mass loss in single, levitated particles under irradiation. The experimental setup has been described previously (Steimer et al., 2015b). In short, an electrically charged aqueous particle (radius $\sim 10\,\mu m$) is injected into an EDB. The balance is of the double ring design (Davis et al., 1990) with a high AC voltage applied to the two-parallel electrode rings and a DC voltage across hyperbolic endcaps. The DC field compensates the gravitational force of the particle and is used as a measure for the mass of the particle. The EDB is placed in a three wall glass chamber, with

110 a cooling liquid (ethanol) pumped through the two inner walls and an insulation vacuum between two outer walls, to control the temperature (T) at the location where the particle levitates. The relative humidity (RH) within the chamber is regulated by adjusting the ratio of a dry and humidified gas flow through the chamber. In the experiments described in this work, we used a typical total flow of 40 sccm and set the total pressure inside the cell at 8×10^4 Pa.

The spherical particles were characterized by two Mie resonance spectroscopy based methods: (i) A narrow bandwidth

115 tunable diode laser (TDL, tuning range $765-781$ nm) was used to determine the refractive index and radius simultaneously with high precision (Steimer et al., 2015b). (ii) Simultaneously, a broad-band LED centered around 640 nm was used to illuminate the particle. And the backscatter signal from the LED is recorded using a spectrograph with a slow scan back-illuminated CCD (charge-coupled device) array detector, to follow the resonance wavelength shift of the particle (Zardini et al., 2006). If we assume refractive index stays constant during the experiment, the radius change of a particle is easily calculated from this

120 resonance wavelength shift:

$$\frac{r(t)}{r_0} = \frac{\lambda_0 + \Delta\lambda(t)}{\lambda_0} = 1 + \frac{\Delta\lambda(t)}{\lambda_0}. \tag{1}$$

We illuminated particles to induce photochemical reaction with either a cw diode laser emitting at 375 nm (LuxX 375-20, Omicron Laserage) or a frequency doubled diode laser emitting at 473 nm (gem 473, Laser Quantum). At the wavelength of 375 and 473 nm, $Fe^{III}(Cit)$ is reported to have a molar absorptivity of 796 and 60.7 $M^{-1}cm^{-1}$, respectively (Pozdnyakov

125 et al., 2008).

In a typical EDB experiment, we let the particle equilibrate to RH and T in a O_2 gas phase for up to 10 hours in the dark before irradiation. Exemplary raw data of an experiment at 46 % RH and 293.5 K is shown in Fig. 2. The measured DC voltage compensating the gravitational force, as well as the radius of the particle deduced from Mie-resonance spectroscopy decreased dramatically during illumination in the first 18 hours, with more than half of the initial mass lost to the gas phase. Note, that

130 the radius and mass loss rates increased as seen in Fig. 2(c). We assumed refractive index and density of the particle did not change upon photochemistry and therefore, the mass loss calculated from the DC voltage could be directly compared with size change by calculating the particle mass remaining ratio,

$$\frac{m(t)}{m_0} = \left\{ \frac{r(t)}{r_0} \right\}^3, \tag{2}$$
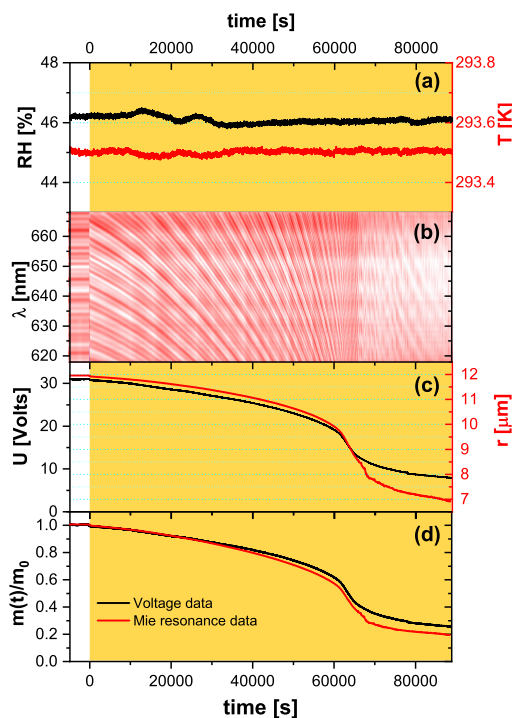
Figure 2. Raw EDB experimental data for a Fe^{III}(Cit)/citric acid (molar ratio of 0.05) particle. (a) Relative humidity (left axis, black) and temperature (right axis, red) of the droplet. (b) Intensity map of low resolution Mie resonance spectra. (c) Black line: DC voltage that compensates gravitational force; Red line: radius of the droplet, with the initial value of the particle radius determined using high resolution Mie resonance spectroscopy (not shown), and the change in radius determined from low resolution Mie resonance data given in (b). (d) Normalized mass remaining ratio deduced from DC voltage (black), and from Mie resonance shift (red) - assuming constant density. Yellow shaded region in panels (a), (c), and (d) indicate the time of laser irradiation with $0.25\,W\,cm^{-2}$ at 375 nm.

where m_0 is the particle mass prior to irradiation. Mass loss derived from both ways independently is shown in Fig. 2(d) and

135   reveal that there is a little difference between the mass loss up to $t \approx 65000$ s, corresponding to when $\frac{m(t)}{m_0} < 0.4$. Therefore, the refractive index and density are mostly governed by those of aqueous citric acid up until the half the particle mass is lost. The total mass loss over 24 hours irradiation is more significant and drops by 80 % for the particular experiment shown in Fig. 2. In addition, we observed the mass loss rate initially was $\sim 1.3\ \%\ h^{-1}$ and increased to $\sim 14\ \%\ h^{-1}$ when 40 % to 60 % of the initial mass was lost. This mass loss acceleration is discussed further in detail with the help of the PRAD model

140   simulations in Subsect. 3.1. At $t \approx 65000$ s, the mass loss slowed down considerably when we observed a distortion in the Mie-resonance pattern (Fig. 2(b) and video in the Supplement). The distortion may be attributable to partial crystallization of iron citrate in the particle, which would explain the slowing photochemical degradation.
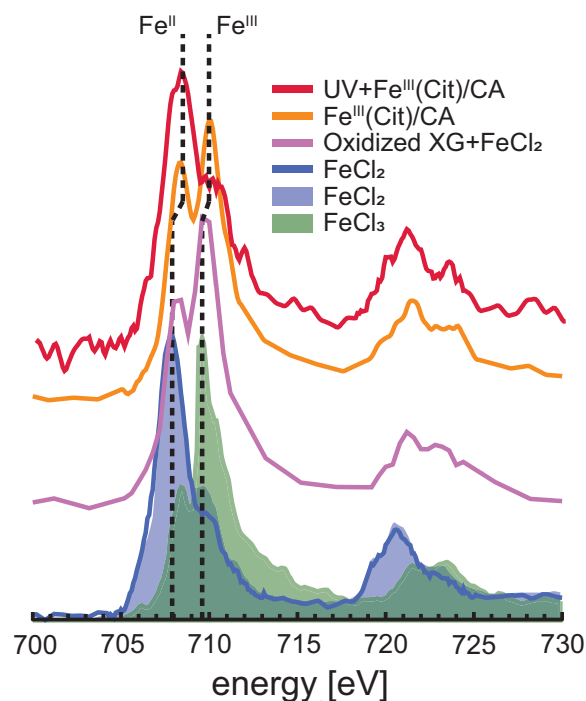
Figure 3. Iron L-edge NEXAFS spectra of Fe^{III}(Cit)/CA particles before and after irradiation with UV light shown as orange and red, respectively. Spectra from mixed xanthan gum (XG) and $FeCl_2$ particles exposed to ozone and from $FeCl_2$ particles are purple and blue lines, respectively, in Alpert et al. (2019). $FeCl_2$ and $FeCl_3$ are blue and green shading, respectively, in Moffet et al. (2012). The vertical dashed lines indicate peak X-ray absorption at 707.9 shifted to 708.3 eV for Fe^{II} and 709.6 shifted to 710.0 eV for Fe^{III}.

2.2 Chemical characterization by STXM/NEXAFS

STXM/NEXAFS measurements were performed at the PolLux endstation located at the Swiss Light Source (SLS) to obtain the

145 Fe oxidation state of particles between 0.2-2 µm in diameter (Flechsig et al., 2007; Frommherz et al., 2010; Raabe et al., 2008). Particles containing Fe^{III}(Cit)/CA were nebulized from aqueous solution with a mole ratio between Fe^{III}(Cit):CA of 1:1. They were dried in air at $RH < 30$ % and impacted onto silicon nitride membranes mounted in portable sample holders. The sample holders were transported to the endstation in an evacuated container and shielded against ambient light. Once there, they were mounted in the PolLux environmental microreactor (Huthwelker et al., 2010), and kept under a total pressure of 1.5×10^4

150 Pa, $T = 293.5K$, $RH = 40$, 50 or 60 %, with a controlled gas flow. Further details of sample preparation are provided in previous literature (Alpert et al., 2019; Huthwelker et al., 2010; Steimer et al., 2014). The microreactor was mounted into a vacuum chamber for in situ STXM/NEXAFS analysis. When desired, the microreactor could operate in vacuum conditions without a gas flow. The transmission of X-ray photons through the particles were measured and converted to optical density, $OD = -\ln(I/I_0)$, where I and I_0 are the transmitted and incident photon flux as a function of X-ray energy. The Fe L-edge

155 absorption was probed over the X-ray energy range of $700 - 735$ eV. Figure 3 shows an example of NEXAFS spectra of

$Fe^{III}(Cit)$/CA particles before (orange) and after (red) irradiation with UV light. X-ray energy calibration was consistently performed using $FeCl_2$ and compared with previous literature for $FeCl_2$ and $FeCl_3$ salts (Moffet et al., 2012) and a mixture of xanthan gum and $FeCl_2$ oxidized by O_3 (Alpert et al., 2019). The peak absorption for iron(II) and iron(III) are at X-ray energies of 708.3 and 710.0 eV. We were capable of resolving peaks separated by 0.4 eV at the Fe L-edge. Ferrous and ferric

160 iron peaks are separated by 1.7 eV and thus, clearly distinguishable. Following a previous procedure (Alpert et al., 2019), we imaged particles at these two energies to determine the OD ratio between them. Then the fraction of Fe^{III} out of total Fe, β, was determined using the parameterization from Moffet et al. (2012). It is important to note that the X-ray energies absorption peaks observed for $FeCl_2$ and $FeCl_3$ were identical for $FeCl_2$ mixed with xanthan gum either unexposed or exposed to O_3 (Alpert et al., 2019). However, we have found that these peaks shifted by about $+0.4$ eV, possibly due to the strong complexation

165 with CA. Small shifts in energy can occur depending on the chemical environment surrounding Fe atoms (Garvie et al., 1994; Moffet et al., 2012). In agreement with Alpert et al. (2019), the peak absorption energies for our particles were independent of RH from 0 % to 60 % within ±0.2 eV. When calculating β, we always imaged particles at at 708.3 and 710.0 eV.

2.3 HO_2 production determined by CWFT

The HO_2 release upon irradiation of a $Fe^{III}(Cit)$/CA thin film was measured by scavenging HO_2 with an excess of NO

170 in a coated wall flow tube (CWFT) reactor (Duran glass, inside diameter 1.2 cm, long 50 cm). The film was composed of $Fe^{III}(Cit)$/CA, and deposited inside the tubular glass flow tube with a thickness between $0.15 - 0.2$ μm and an error of about 20 %. Details of the film preparation are described previously (Corral Arroyo et al., 2018; González Palacios et al., 2016). Seven UV lamps (UV-A range, Philips Cleo Effect) were mounted surrounding the glass reactor held at 298.15 K. The total light output between $300 - 590$ nm was 210 W m^{-2}. The flows of N_2, O_2, and NO passing through the reactor

175 were controlled. The NO concentration during CWFT photochemical experiments was in excess ($> 10^{13}$ molecules cm^{-3}) to efficiently scavenge 99 % of HO_2 produced by the film. The concentration of NO was tracked by a chemiluminescence detector (Ecophysics CLD 77 AM). In an example CWFT experiment at $RH = 29.3$ %, a clear NO loss was observed when UV lights were switched on as shown in Fig. 4, which was due to the release of HO_2 radicals into the gas phase and reaction of NO with HO_2 forming NO_2 and OH·. OH· is then scavenged by NO producing HONO. The production of HONO was

180 routinely checked as described in González Palacios et al. (2016). Therefore, the production rate of HO_2, P_{HO_2}, was calculated from the loss rate of NO assuming a 2:1 ratio to HO_2 conversion:

$$P_{HO_2} = \frac{[NO] \times \text{flow}}{2S_{\text{film}}}, \tag{3}$$

where [NO] is the loss of gas-phase concentration of NO in molecules cm^{-3}, flow is the volumetric gas flow in the CWFT in cm^3 s^{-1}, and S_{film} is the surface area of the film in cm^2.

2.4 Development of the PRAD model

185

We developed a photochemical reaction and diffusion (PRAD) model to interpret our experiments and to understand any feedbacks between transport limitations and photochemistry, especially under low RH conditions, corresponding to high viscosity
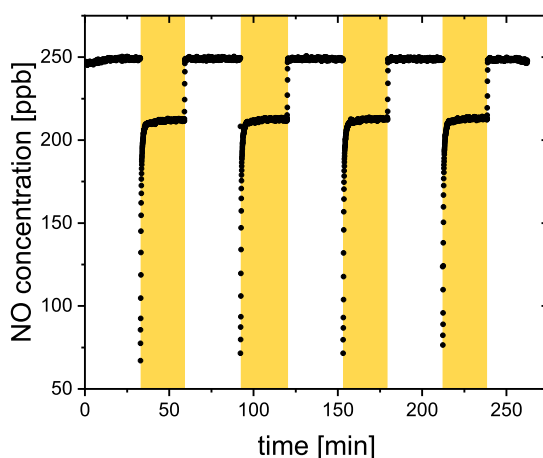
Figure 4. NO concentration raw data from CWFT film containing $Fe^{III}(Cit)$/CA (molar ratio of 0.07) with lamps on (yellow shaded region) and off at 29.3 % RH and 298.15 K.

of the particle phase. The PRAD model consists of two modules: a detailed chemical process module, treating equilibria and chemical reactions, and a transport module handling the physical transport of all species (including diffusion in the aqueous phase as well as gas-particle phase partitioning). As illustrated in Fig. 5, the PRAD model devides a spherical droplet into a number of shells, n, which exchange molecules after each chemical time step. Shell thickness and numbers of shells were adjusted to enable the resolution of steep concentration gradients within a reasonable computation time. The volume of each shell was constant instead of the thickness and the shells become thinner and thinner from the center to the surface of the particle. For each shell and at each time step, we first calculated the composition using the thermodynamic equilibria of the $Fe^{III}(Cit)$/CA system, as listed in Table 2. Then the Newton-Raphson method (Burden and Faires, 2011) was used to calculate the turnover and the concentration of products and reactants over time for the chemical reactions listed also in Table 2 with a fixed time step of 0.2 s. After each time step diffusion of all species between the shells and the evaporation of products (or condensation of the reactant O_2) were computed. The time step, Δt, for physical transport processes was determined dynamically to ensure both numerical stability and computational efficiency.

For each species, the molar flux from shell i to the next shell $i+1$ was calculated as

$$f_i = -4\pi r_i^2 D_l \frac{dc}{dr}\bigg|_{r=r_i} = -4\pi r_i^2 D_l \frac{c_{i+1} - c_i}{0.5(r_{r+1} - r_{i-1})}; \qquad \forall i \in \{1, 2, ..., n-1\}, \tag{4}$$

where D_l is the liquid phase diffusion coefficient of the corresponding species. Shell i extends from r_{i-1} to r_i, while shell $i+1$ extends from r_i to r_{i+1}, with r being the distance from the particle center. In Eq. (4), c is the molar concentration in each shell of the aqueous particle, defined as

$$c_i = \frac{N_i}{V}; \qquad \forall i \in \{1, 2, ..., n\}, \tag{5}$$
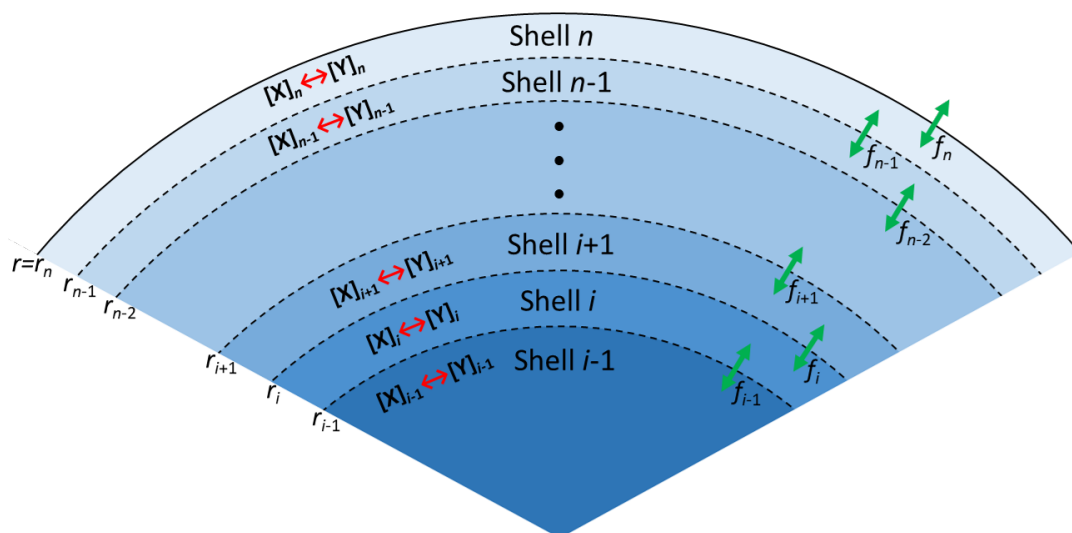
Figure 5. Schematic illustration of the PRAD model. Shells, transport fluxes (green arrows), and chemical processes (red arrows) of each species. The particle is radially symmetric with the surface of the particle marked as r_n.

where N_i is moles of a particular species in shell i, and V is the total volume of a shell.

At the outermost shell n, the gas-particle phase partitioning of each species was determined by the modified Raoult's law. The flux from shell n into the gas phase, f_n, was calculated to be

$$f_n = -4\pi r_n D_g \frac{p_{\text{partial}} - p_{\text{vapor}}}{RT}, \tag{6}$$

210   where D_g is the gas phase diffusion coefficient of the corresponding species, and R is the gas constant. p_{partial} is the partial pressure of the species in the gas phase at infinite distance from the particle. Based on Henry's law, vapor pressure of the species p_{vapor} is defined as

$$p_{\text{vapor}} = \frac{c_n}{H}, \tag{7}$$

where c_n is the molar concentration in the outermost shell n, and H is the Henry's law coefficient. Substituting Eq. (7) into
215   Eq. (6) leads to

$$f_n = -4\pi r_n D_g \left(\frac{p_{\text{partial}}}{RT} - \frac{c_n}{HRT} \right). \tag{8}$$

We calculated the partial pressure of H_2O from RH, and took the partial pressure of O_2 based on the total pressure and the fraction of O_2 gas flow used in experiments. For other species, p_{partial} is negligible and assumed to be zero. So for all species other than H_2O and O_2, f_n simplifies to

220   $$f_n = -4\pi r_n D_g \left(0 - \frac{c_n}{HRT} \right) = 4\pi r_n D_g \frac{c_n}{HRT}. \tag{9}$$

Based on the calculated fluxes, the change in moles, ΔN_i, of each species in Δt was given by

$$\Delta N_i = (f_{i-1} - f_i)\Delta t; \qquad \forall i \in \{1, 2, ..., n\}, \tag{10}$$

from which the concentration and corresponding shell thickness using the molar volume of each species were recalculated for the next time step.

225   The chemical loss rate of O_2 was treated in the liquid phase diffusion module instead of in the chemical module, since the loss can be very fast and its life time can be smaller than 10^{-6} s. If O_2 loss due to reaction was determined in the chemical module, a chemical time step of 10^{-6} s would result in extensive computational time beyond what is reasonable for this study. Therefore, within each liquid phase diffusion time step, in addition to the physical transport, the chemical loss of O_2 molecules was calculated in each shell

230
$$\frac{dN_i}{dt} = -k_{O_2} N_i; \qquad \forall i \in \{1, 2, ..., n\}. \tag{11}$$

Integration yields

$$N_i = N_i e^{-k_{O_2}\Delta t}; \qquad \forall i \in \{1, 2, ..., n-1\}, \tag{12}$$

where k_{O_2} is total chemical reaction rate of O_2. In the outermost shell n, O_2 molar concentration is assumed to be at steady state all times, meaning that the chemical loss of O_2 is always compensated by the condensation of O_2 from the gas phase:

235
$$-k_{O_2} N_{n,O_2} = -4\pi r_n D_g \left(\frac{p_{\text{partial},O_2}}{RT} - \frac{c_n}{H_{O_2} RT} \right). \tag{13}$$

Substituting Eq. (5) in Eq. (13), we calculate the moles of O_2 in this shell, N_{n,O_2}, as

$$N_{n,O_2} = \frac{p_{\text{partial},O_2}}{k_{O_2} RT/(4\pi r_n D_g) + 1/(H_{O_2} V_n)}. \tag{14}$$

where H_{O_2} is Henry's law coefficient of O_2.

All iron containing compounds and all free ions are considered not to evaporate from the particle phase. All other species 240 have Henry's law coefficients given in Table 2. If the evaporation rate of some species is fast enough, then their concentration in the outermost shell n can always be at steady state, which means

$$f_{n-1} = f_n, \tag{15}$$

that is,

$$-4\pi r_{n-1}^2 D_l \frac{c_n - c_{n-1}}{0.5(r_n - r_{n-2})} = 4\pi r_n D_g \frac{c_n}{HRT}. \tag{16}$$

245   From Eq. (16), c_n can be deduced to be

$$c_n = c_{n-1} \frac{1}{1 + 0.5(r_n - r_{n-2})r_n D_g/(HRT r_{n-1}^2 D_l)}. \tag{17}$$

And the number of molecules of the volatile species in the outermost shell N_n as

$$N_n = c_n V_n. \tag{18}$$

We have parameterized aqueous and gas phase diffusion coefficients, D_l^j and D_g^j, respectively, for all species j given in
250 Appendix A1 and A2. There are several other assumptions and approximations made to adapt this model to the aqueous
$Fe^{III}(Cit)/CA$ system:

1. We set water activity in the particle phase always in equilibrium with the gas phase, since the RH of the gas phase did
   not change during each experiment.

2. The bulk accommodation coefficients of all species were assumed to be 1.

255 3. Neglecting the influence of $Fe^{III}(Cit)$, the water activity was taken from that of CA (a_w^{CA}), which has been determined
   from the mass fraction of CA, W_{CA}, by Lienhard et al. (2012)

$$a_w^{CA} = \frac{1 - W_{CA}}{1 + q \cdot W_{CA} + r \cdot W_{CA}^2}, \tag{19}$$

   with

$$q = -3.16761 + 0.01939T - 4.02725 \times 10^{-5}T^2, \tag{20}$$

260 and

$$r = 6.59108 - 0.05294T + 1.06028 \times 10^{-4}T^2, \tag{21}$$

   The water activity of citrate (a_w^{Cit}) was calculated using the same equation

$$a_w^{Cit} = \frac{1 - W_{Cit}}{1 + q \cdot W_{Cit} + r \cdot W_{Cit}^2}, \tag{22}$$

   where the mass fraction of citrate W_{Cit} was treated in two fractions: citrate without Fe and citrate containing Fe. The
265   water activity of an aqueous 1 M $Fe^{III}(Cit)$ solution was determined using a water activity meter (AquaLab water,
   Model 3B, Decadon Device, USA) at room temperature. We found this water activity corresponds to that of a 0.81 M
   aqueous CA solution. Therefore, for calculating water activity, all iron containing citrate complexes (no matter Fe^{II} or
   Fe^{III}) were treated with a reduced concentration: namely with a factor of 0.81 of the corresponding citrate molarity.
   Hence, the overall amount of citrate was calculated as

270 $$n_{Cit}^* = n_{Cit} + 0.81 n_{FeCit}, \tag{23}$$

   accordingly and W_{Cit} was determined following

$$W_{Cit} = \frac{M_{Cit} \cdot n_{Cit}^*}{M_{Cit} \cdot n_{Cit}^* + M_{H_2O} \cdot n_{H_2O}}, \tag{24}$$

where M_{Cit} and $M_{\mathrm{H_2O}}$ are the molar mass of CA and water, respectively. For other species j, the contribution to the water activity is proportional to their molar volume (MV_j), so that in total,

$$a_{\mathrm{w}} = a_{\mathrm{w}}^{\mathrm{CA}} + a_{\mathrm{w}}^{\mathrm{Cit}} + \frac{MV_{\mathrm{H_2O}}}{MV_{\mathrm{H_2O}} + \sum_j MV_j}. \tag{25}$$

4. $Fe^{\mathrm{III}}(\mathrm{Cit})$ photolysis, decarboxylation and oxidation of the alcohol group in presence of O_2 yields the compounds $\mathrm{O{=}C(CH_2COO)_2^{2-}}$ or $\mathrm{O{=}C(CH_2COOH)_2}$, which are C_5 species. We assumed that half of C_5 species undergoes photochemical reactions to produce CO_2 and compounds with $2-4$ carbon atoms, C_4, C_3 and C_2 (see reactions R11−R15 shown in Table 2), all of which are capable of being released to the gas phased depending on their solubility.

5. We estimated the quantum yield in reactions R1 and R2 in Table 2, as $\Phi = 1.0$ at $\lambda = 375$ nm and $\Phi = 0.002$ at $\lambda = 473$ nm (Dou et al., 2019), and we parameterized Φ as a function of wavelength, λ:

$$\Phi = \frac{e^{-0.145(\lambda-430)}}{1 + e^{-0.145(\lambda-430)}}. \tag{26}$$

In total, the PRAD model includes 13 equilibria and 17 chemical reactions among 32 species, as well as their condensed phase diffusivities and Henry's law coefficients. Some of these parameters are known from previous studies (see Tables 1 and 2 for references), while others are not known and difficult to estimate. For instance, even though absorption spectra of $Fe^{\mathrm{III}}(\mathrm{Cit})$ has been measured in aqueous solution (Pozdnyakov et al., 2012), the corresponding quantum yield has not, which leaves the photolysis rate of $Fe^{\mathrm{III}}(\mathrm{Cit})$, j, unknown. Also, there are no data reported of the diffusivity of O_2 in aqueous citric acid solutions, and the chemical reaction rate of the oxidation of the Fe^{II}-citrate complex by O_2 is quite uncertain (Gonzalez et al., 2017). In order to find the optimal parameter set, we compared experimental data of the three setups taken under well-controlled conditions with model predictions and tuned the unknown parameters manually. Comparison of the refined model with experimental data are shown in the next section.

Table 1. Liquid phase diffusivity factors (normalized to water) and Henry's law coefficients (Sander, 2015) of major species in $Fe^{III}(Cit)$ photochemistry system.

number	name	formula	l_f^j†	H_0 (M atm^{-1})‡	Q‡
1	water	H_2O	1	1	1
2	cit total	-	-	-	-
3	ferric (Fe^{III}) total	-	-	-	-
4	ferrous (Fe^{II}) total	-	-	-	-
5	citric acid (CA)	$(CH_2COOH)_2C(OH)(COOH)$ /H_3Cit	1.20×10^{-6}	infinite	10000
6	dihydrogen citrate	$(CH_2COOH)_2C(OH)(COO)^-$ /H_2Cit^-	1.20×10^{-6}	infinite	10000
7	hydrogen citrate	$(CH_2COOH)C(OH)(CH_2COO)(COO)^{2-}$ /$HCit^{2-}$	1.20×10^{-6}	infinite	10000
8	citrate	$C(OH)(CH_2COO)_2(COO)^{3-}$ /Cit^{3-}	1.20×10^{-6}	infinite	10000
9		$Fe^{III}(Cit)(OH)^-$	3.92×10^{-7}	infinite	10000
10		$Fe^{III}(HCit)^+$	5.04×10^{-7}	infinite	10000
11	ferrous citrate	$Fe^{II}(HCit)$	5.04×10^{-7}	infinite	10000
12	ferric citrate	$Fe^{III}(Cit)$	5.04×10^{-7}	infinite	10000
13	ferric ion	Fe^{3+}	3.78×10^{-5}	infinite	10000
14		$Fe^{III}(OH)^{2+}$	1.18×10^{-5}	infinite	10000
15	ferrous ion	Fe^{2+}	3.78×10^{-5}	infinite	10000
16	hydrogen ion	H^+	-	-	-
17	hydroxide ion	OH^-	-	-	-
18	hydroperoxyl radical	HO_2	1.13×10^{-4}	4×10^4	5900
19	superoxide radical	O_2^-	-	-	-
20	radicals	$OH-\cdot C(CH_2COO)_2^{2-} + OH-C(CH_2COOH)_2$	2.69×10^{-6}	infinite	10000
21	hydroxyl radical	$\cdot OH$	-	-	-
22	hydrogen peroxide	H_2O_2	1.07×10^{-4}	8.3×10^5	7400
23	oxygen	O_2	1.20×10^{-4}	3.5×10^{-2}	1500
24	carbon dioxide	CO_2	depends on a_w	3.4×10^{-1}	2400
25	acetone	CH_3COCH_3	1.18×10^{-5}	30	4600
26	unk prod C_4	C_4	5.30×10^{-6}	1×10^5	6000
27		$O=C(CH_2COO)_2^{2-} + O=C(CH_2COOH)_2$	1.95×10^{-6}	infinite	8000
28	acetic acid	CH_3COOH	3.23×10^{-5}	4.1×10^3	6300
29		$Fe^{II}[O=C(CH_2COO)_2]$	7.22×10^{-7}	infinite	10000
30	unk prod C_5	C_5	2.69×10^{-6}	1×10^7	8000
31	unk prod C_5	C_5_stable	2.69×10^{-6}	5×10^8	8000

† l_f^j is a factor of the diffusion coefficient of each species j normalized to that of water.

‡ Henry's law is described as a function of temperature T: $H = H_0 e^{\frac{Q}{T} - \frac{Q}{T_0}}$.

Table 2. Compilation of equilibria, chemical reactions, and corresponding rate constants in $Fe^{III}(Cit)$ photochemistry system.

number	reactions	$K_{eq}/k_r/\sigma$	sources
E1	$H_2O \rightleftharpoons OH^- + H^+$	1×10^{-14} M	
E2	$H_3Cit \rightleftharpoons H_2Cit^- + H^+$	7.5×10^{-4} M	Martell and Smith (1982)
E3	$H_2Cit^- \rightleftharpoons HCit^{2-} + H^+$	1.7×10^{-5} M	Martell and Smith (1982)
E4	$HCit^{2-} \rightleftharpoons Cit^{3-} + H^+$	4.0×10^{-7} M	Martell and Smith (1982)
E5	$Fe^{3+} + Cit^{3-} \rightleftharpoons Fe^{III}(Cit)$	1.58×10^{13} M^{-1}	tuning parameter
E6	$Fe^{3+} + Cit^{3-} + H_2O \rightleftharpoons Fe^{III}(Cit)(OH)- + H^+$	8.35×10^{7} M^{-1}	tuning parameter
E7	$Fe^{3+} + HCit^{2-} \rightleftharpoons Fe^{III}(HCit)^+$	2.51×10^{7} M^{-1}	tuning parameter
E8	$Fe^{2+} + HCit^{2-} \rightleftharpoons Fe^{II}(HCit)$	1.935×10^{10} M^{-1}	tuning parameter
E9	$Fe^{3+} + H_2O \rightleftharpoons Fe^{III}(OH)^{2+} + H^+$	4.57×10^{-3} M	Smith and Martell (1976)
E10	$O_2^- + H^+ \rightleftharpoons HO_2$	6.3×10^4 M^{-1}	Bielski et al. (1985)
E11	$Fe^{2+} + O=C(CH_2COO)_2^{2-} \rightleftharpoons Fe^{II}[O=C(CH_2COO)_2]$	2×10^3 M^{-1}	tuning parameter
E12	$2H^+ + OH-\cdot C(CH_2COO)_2^{2-} \rightleftharpoons OH-\cdot C(CH_2COOH)_2$	1.5×10^6 M^{-2}	tuning parameter
E13	$2H^+ + O=C(CH_2COO)_2^{2-} \rightleftharpoons O=C(CH_2COOH)_2$	1.5×10^6 M^{-2}	tuning parameter
R1	$Fe^{III}(Cit) + h\nu \rightarrow Fe^{2+} + OH-\cdot C(CH_2COO)_2^{2-} + CO_2$	3.0×10^{-18} (at 375 nm) or	Pozdnyakov et al. (2012)
R2	$Fe^{III}(Cit)(OH)- + h\nu \rightarrow Fe^{2+} + OH-\cdot C(CH_2COO)_2^{2-} + OH^- + CO_2$	2.3×10^{-19} (at 473 nm) cm^2	
R3	$OH-\cdot C(CH_2COO)_2^{2-} + O_2 \rightarrow O=C(CH_2COO)_2^{2-} + O_2^- + H^+$	1×10^6 $M^{-1}\,s^{-1}$	Hug et al. (2001)
R4	$OH-\cdot C(CH_2COO)_2^{2-} + O_2 \rightarrow O=C(CH_2COO)_2^{2-} + O_2^- + H^+$	1×10^6 $M^{-1}\,s^{-1}$	Hug et al. (2001)
R5	$HO_2 + HO_2 \rightarrow H_2O_2 + O_2$	2.5×10^7 $M^{-1}\,s^{-1}$	tuning parameter
R6	$Fe^{2+} + O_2^- (+2H^+) \rightarrow Fe^{3+} + H_2O_2$	1×10^7 $M^{-1}\,s^{-1}$	Rush and Bielski (1985)
R7	$Fe^{2+} + HO_2(+H^+) \rightarrow Fe^{3+} + H_2O_2$	1.2×10^6 $M^{-1}\,s^{-1}$	Rush and Bielski (1985)
R8	$Fe^{2+} + H_2O_2 \rightarrow Fe^{3+} + \cdot OH + OH^-$	$76\,M^{-1}\,s^{-1}$	Walling (1975)
R9	$Fe^{2+} + \cdot OH \rightarrow Fe^{III}(OH)^{2+}$	4.3×10^8 $M^{-1}\,s^{-1}$	Christensen and Sehested (1981)
R10	$Fe^{II}(HCit) + O_2 \rightarrow Fe^{III}(Cit) + HO_2$	0.05 $M^{-1}\,s^{-1}$	tuning parameter
R11	$C_5 + h\nu \rightarrow C_3 + 2CO_2$	1×10^{-21} cm^2	tuning parameter
R12	$C_4 + h\nu \rightarrow C_3 + CO_2$	1×10^{-20} cm^2	tuning parameter
R13	$C_5 + h\nu \rightarrow C_2 + C_3$	1×10^{-22} cm^2	tuning parameter
R14	$C_4 + h\nu \rightarrow C_2 + C_2$	1×10^{-21} cm^2	tuning parameter
R15	$C_5 + h\nu \rightarrow C_4 + CO_2$	1×10^{-20} cm^2	tuning parameter
R16	C_5_stable fraction	0.5	tuning parameter
R17	radical self reaction	0	tuning parameter

3 Comparisons between experimental measurements and model simulations

3.1 The effect of RH on photocatalytic degradation efficiency

We performed experiments with single, levitated particles under continuous UV irradiation (375 nm) in an O_2-atmosphere

295 at different RH to access the effects of RH on the photocatalytic cycle shown in Fig. 1, and tested the model performance under these conditions. Qualitatively, a continuous decrease of particle mass and size is expected to occur due to evaporation of volatile products, as shown in Fig. 2. Figure 6 shows the fraction of particle mass remaining with the irradiation time at three different RH, calculated from resonance wavelength shifts (Eqs. (1) and (2)). Clearly, particle mass was lost to the gas phase with time due to the evaporation of photochemical products and similar to Fig. 2, all data show a very significant acceleration of

300 mass loss with time. After tuning some of the parameters of the model as discussed further below, the PRAD model simulations reproduces our data with a very similar trend and magnitude over all, which gives us confidence that the PRAD model captures the essential chemistry and transport during irradiation. However, the model is not able to capture the full degree of acceleration of the degradation rate, as it does not attempt to include the complete multi-generational oxidation chemistry at the level of individual components after initial radical production. The degradation progresses were faster at higher RH. At lower RH, the

305 particle was expected to be more viscous, diffusion coefficients were expected to be lower, products were generated at a lower rate, and volatile products moved more slowly to the surface to evaporate. More importantly, O_2 taken up by the particle from the gas phase diffused more slowly into the bulk of the particle at lower RH, thus less HO_2 and H_2O_2 formed and less Fe^{II} could be re-oxidized from the surface to the center of the particle. The observed gradient in Fe^{III} fraction, β, and the modelled gradients in O_2 and ROS in the particle have been shown with radial profiles in Alpert et al. (2020). This resulted in fewer

310 photochemically active Fe^{III} complexes available for photocatalytic degradation. The characteristic degradation time shortened by a factor of 5.5 when RH increased from 46 % and 61 %, which demonstrates that photochemical cycling is highly sensitive to the microphysical conditions. The diffusivity of O_2 must have significantly impacted re-oxidation reaction rates. In addition, the diffusion coefficients of both Fe^{II} and Fe^{III} species increases with RH. Therefore, the molecular transport between both iron and oxygen reactants increases causing a highly non-linear trend in increasing mass loss with increasing RH.

315 3.2 Determination of iron(III) reduction rate and iron(II) re-oxidation rate by STXM/NEXAFS

In STXM/NEXAFS experiments, the freshly prepared $Fe^{III}(Cit)$ mixed with CA at $x = 1.0$ particles were irradiated to determine the $Fe^{III}(Cit)$ photolysis rate, as shown in Fig. 7. Each experimental data point is the average Fe^{III} fraction from $16 - 36$ individual particles. Fitting an exponential function, $\beta = \beta_0 e^{j_{obs}t}$, yields $\beta_0 = 0.93 \pm 0.09$ and a first order decay rate of $j_{obs} = 0.08 \pm 0.01 \text{ s}^{-1}$. The LED power at the sample was measured to be $5.9 \pm 0.6 \text{ mW}$ in total and had a Gaussian spectral

320 profile between $361 - 374 \text{ nm}$ at full width-half max. When mounting the UV fiber optics and collimator lens for multiple samples, the illuminated area had a circle equivalent diameter of $5 \pm 1.5 \text{ mm}$. Using the absorption cross section calculated from the molar attenuation coefficient (Pozdnyakov et al., 2008), $\Phi = 1.0$ and propogating all uncertainties yields a photochemical reaction rate of $j_{calc} = 0.20 \pm 0.12 \text{ s}^{-1}$, which is in agreement with j_{obs}. This implies that assuming a quantum yield of 1 at
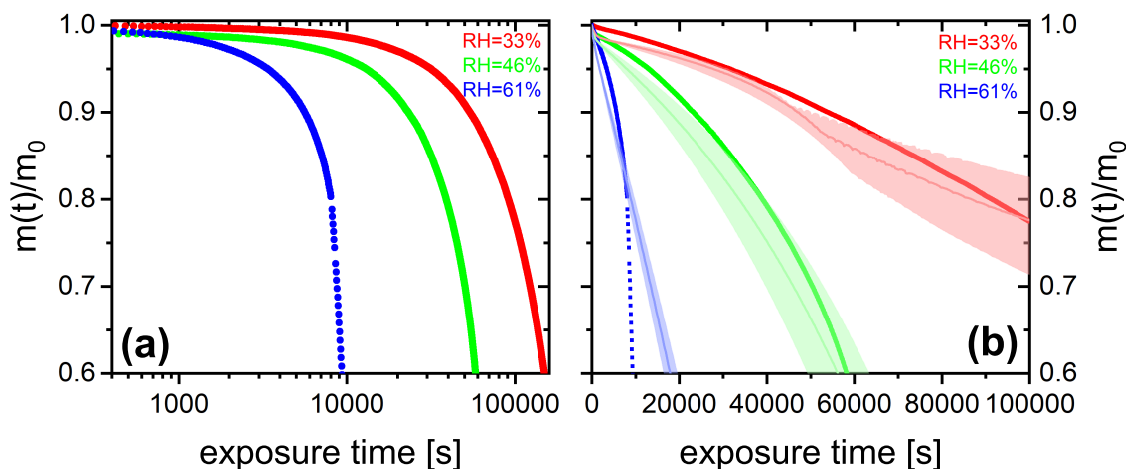
Figure 6. (a) $Fe^{III}(Cit)$/CA (molar ratio 0.05) particle mass change with irradiation time (log scale) at different RH: 33 % (black), 46 % (red), and 61 % (blue). The irradiation wavelength was 375 nm, its intensity was 0.25 $W\,cm^{-2}$, and the experimental temperature was 293.5 K. (b) EDB experimental data in (a) with PRAD outputs at corresponding RH (with ± 2 % RH uncertainty shown as shaded area) as a function of irradiation time (linear scale).

these UV wavelengths is reasonable. This calculated value for the photochemical reaction rate was used in the PRAD model
325 for analyzing the STXM/NEXAFS experiments.

In a different set of experiments, we irradiated particles in a He and O_2 atmosphere and at a fixed RH for 15 min to reduce Fe^{III} to Fe^{II}. The UV light was then switched off to allow re-oxidation in the dark while measuring β over time. Figure 8 shows β as a function of time at $RH = 40$, 50, and 60 %. Clearly, the Fe^{III} fraction increased significantly slower with time at dryer conditions. While particles were observed to re-oxidize completely within about 6 hours at 60 % RH, no significant
330 re-oxidation occurred on this timescale for the particles exposed to only 40 % RH. Modelling the re-oxidation with the PRAD model yields very satisfactory agreement, indicating that the diffusivity parameterizations of the model are capturing the RH dependence of the molecular transport in the viscous matrix.

3.3 Determination of iron(II) re-oxidation rate with single, levitated particle using EDB

As the experiments with single, levitated particles yield only bulk properties and not the oxidation state of iron-citrate directly,
335 we designed a dedicated experimental procedure to indirectly determine the re-oxidation rate of Fe^{II}. We used multiple irradiation and re-oxidation repetitions as shown schematically in Fig. 9. Initially, we exposed a newly injected $Fe^{III}(Cit)$/CA aqueous particle to blue laser irradiation (473 nm, 4 $W\,cm^{-2}$) in pure N_2 for 500 s to ensure all Fe^{III} was reduced through photolysis reactions R1 and R2 (listed in Table 2). As previously described, these reactions led to CO_2 production with subsequently loss of CO_2 to the gas phase, which was observed as a shift in the Mie-resonance wavelength. This shift is shown
340 in Fig. 2(b) and on an enlarged scale in Fig. 10. After irradiation, we switched the gas flow from N_2 to O_2 in the dark, and
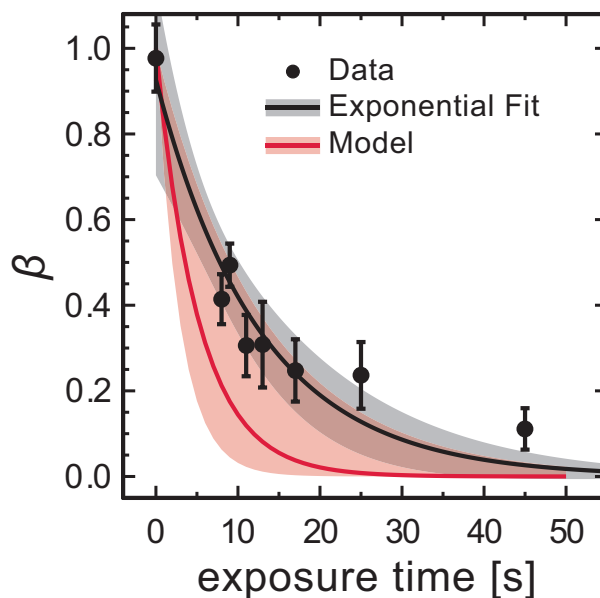
Figure 7. Loss of Fe^{III} in $Fe^{III}(Cit)$/CA (molar ratio of 1) particles as a function of light exposure time determined using STXM/NEXAFS at 293.5 K. Each data point is the average Fe^{III} fraction over about $16 - 36$ individual particles. An exponential fit, $\beta = \beta_0 e^{j_{obs}t}$, yields for the initial condition is $\beta_0 = 0.93 \pm 0.09$ and a first order decay rate of $j_{obs} = 0.08 \pm 0.01\ s^{-1}$. The black shading indicates 95 % confidence on the exponential fit. The PRAD model prediction and uncertainty are given as red solid line and shading, respectively, and uses a calculated decay rate of $j_{calc} = 0.20 \pm 0.12\ s^{-1}$.

Fe^{II} was oxidized back to Fe^{III} over time in this period, either by ROS (R6−R9) or directly by O_2 (R10). After a desired time spent in O_2, the gas flow was switched back to N_2 followed by irradiation to repeat the photolysis step done initially. The ratio of the Mie-resonance wavelength shift of the two photolysis steps was set proportional to the ratio of re-oxidized Fe^{III}/Fe_{tot}. These two steps (i.e., photolysis in N_2 and re-oxidation in O_2) were repeated several times, but between each irradiation the

345   particle was exposed to O_2 for different time periods. Following this procedure we intended to map out the characteristic time for re-oxidation at various RH.

    An example of the corresponding raw data (293.5 K and 48 % RH) and retrieved oxidation state is shown Fig. 10. Black circles indicate the first irradiation step with a fresh $Fe^{III}(Cit)$/CA particle, and red circles indicate the irradiation step that followed the particle after exposure to O_2 for 45 min in the dark. Clearly, the resonance wavelength decreased more during

350   the first irradiation than the second. Therefore, we can conclude unambiguously that the $Fe^{III}(Cit)$/CA particle initially had more Fe^{III} than what could be re-oxidized in O_2 for 45 min. Quantitative scaling however, requires knowledge of the initial Fe^{III} fraction. Our experiments showed that long exposure (tens of hours) to O_2 yielded larger Mie-resonance shifts than those of the initial photolysis of the freshly prepared particle. This indicated that the initial Fe^{III} fraction was less than 1.0. Hence, we normalized the Fe^{III} fraction accordingly to the data at long (> 15 hours) exposure times. For the experiment included in

355   Fig. 10 for example, the initial Fe^{III} fraction of the particle was 0.76, indicating that the particle has been partially reduced
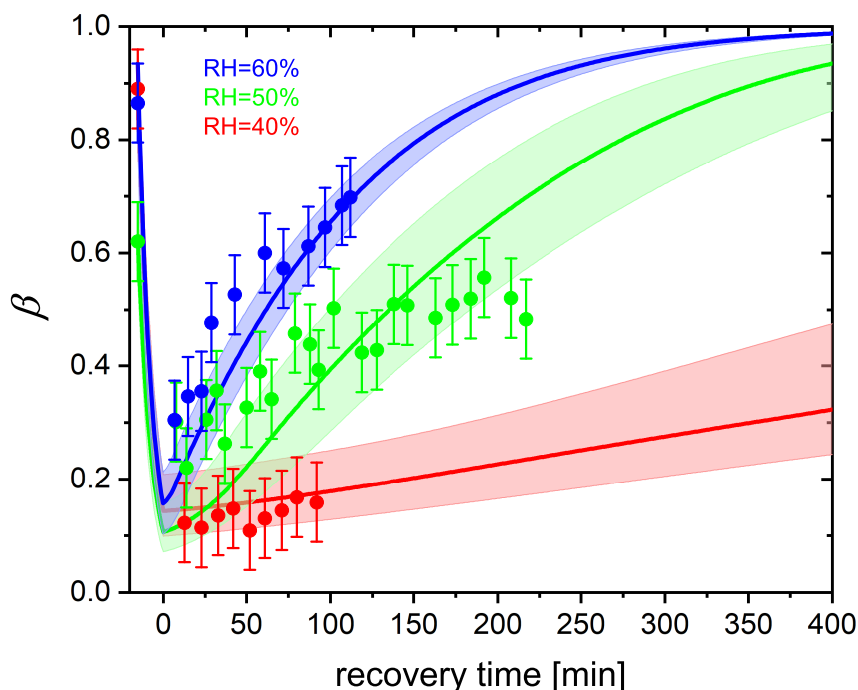
Figure 8. Re-oxidation of Fe^{III} as a function of exposure time in O_2 from STXM observations. Time before 0 represents initial 15 min irradiation procedure under He. Fe^{III}(Cit)/CA (molar ratio of 1) particles at 293.5 K with 40 % RH (red dots), 50 % RH (green dots), and 60 % RH (blue dots). Lines: red (40 % RH), green (48 % RH), and blue (65 % RH) are the Fe^{III} fractions predicted using the PRAD model, the shaded areas indicate model output assuming ±2 % RH, ±0.07 initial Fe^{III} fraction, and ±1.8 % light intensity uncertainty in the STXM experimental conditions.
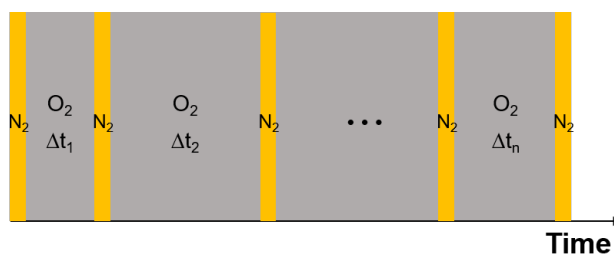
Figure 9. Schematic of the experimental procedure to investigate the re-oxidation rate of Fe^{II}. Orange columns represent laser irradiation (473 nm, 4 W cm^{-2}), each irradiation takes place in a N_2 atmosphere for a period of 500 s; grey columns mark the recovery process in a O_2 atmosphere in the dark, here the time interval is varied. For details see text.
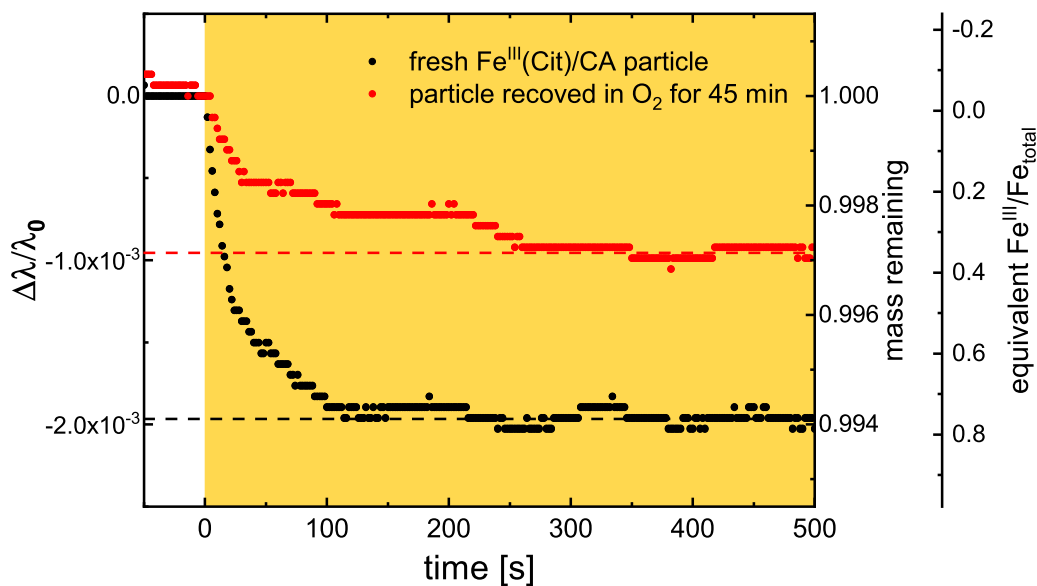
Figure 10. Temporal evolution of two Mie resonance wavelengths shifts and particle mass changes normalized to the wavelength and mass prior irradiation; the experiment was done at 48 % RH and 293.5 K. The orange area marks the time with irradiation (473 nm, 4 W cm^{-2}). Black: first irradiation with a fresh Fe^{III}(Cit)/CA particle in N$_2$, red: irradiation right after the particle recovered in O$_2$ for 45 min in the dark. Two horizontal dashed lines are indicating the final mass remaining after CO$_2$ loss to the gas phase. For explanation of scaling of the third axis, indicating the equivalent Fe^{III}/Fe$_{tot}$ ratio, see text.

during sample preparation. After the particle has been totally photoreduced, exposure to O$_2$ for 45 min did not re-oxidize all reduced Fe^{II} to Fe^{III}, but only 0.36 Fe^{III} has been recovered (as shown with two horizontal dashed lines in Fig. 10).

Another set of experiments was done by starting with freshly injected Fe^{II}(HCit)/CA particles instead of Fe^{III}(Cit)/CA. The only difference in experimental procedure, compared to what is described above, is that there is no first irradiation step.
360   Instead, the particle is initially exposed to O$_2$ in the dark for a certain time interval, during which Fe^{II} is oxidized only directly by O$_2$ (reaction R10). Afterwards, the same irradiation and recovery procedures as reported above were taken. The equivalent Fe^{III} fractions of all experiments are shown in Fig. 11. Any uncertainty in the normalization of an individual experiment will cause a corresponding uncertainty in the normalized mass loss, which made estimating the uncertainty for individual data points impossible. Nevertheless, from the complete data set, it was evident that with longer time intervals in O$_2$, more Fe^{III}
365   was recovered. At 48 % and 65 % RH, about 10 hours and 3 hours exposure to O$_2$, respectively, was sufficient for all Fe^{II} to be re-oxidized, while at 24 % RH, the recovery even after 25 h was not yet complete. The general trend is consistent with
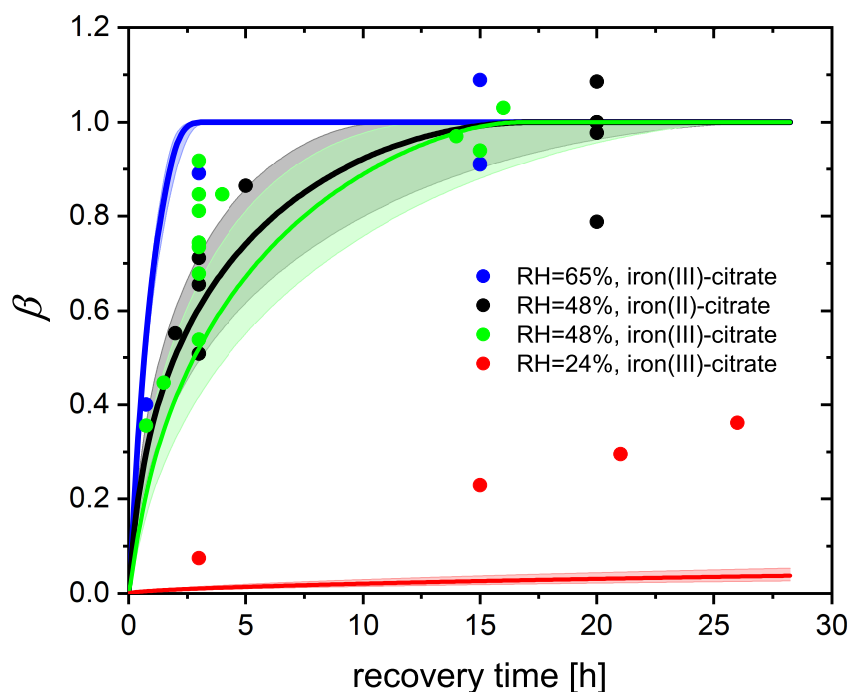
Figure 11. Fe^{III} fraction after different time intervals of recovery in O_2 from EDB observations. $Fe^{III}(Cit)$/CA (molar ratio of 0.05) particles at 293.5 K with 24 % RH (red dots), 48 % RH (green dots), and 65 % RH (blue dots). Black dots: experiments with $Fe^{II}(HCit)$/CA particles at 48 % RH. Lines: red (24 % RH), black (48 % RH), and blue (65 % RH) are the Fe^{III} fractions predicted using the PRAD model, the shaded areas indicate model output assuming ± 2 % RH uncertainty in the EDB experimental conditions.

our observation in the STXM/NEXAFS experiments (Subsect. 3.2) and can be attributed to molecular diffusion limitations at lower RH: it takes more time for O_2 to diffuse into the particle, and for Fe^{II} to diffuse out to the surface of the particle to react with O_2. It was also evident from these data that Fe^{II} re-oxidized by O_2 is as important as Fe^{II} re-oxidized by radicals and

370   peroxides as there is no significant difference between the experiments starting from $Fe^{II}(HCit)$/CA compared to those with $Fe^{III}(Cit)$/CA.

By tuning the direct oxidation rate of $Fe^{II}(HCit)$ by O_2 (R10) and the diffusivity of O_2, we are able to model the recovery rate at different RH using the PRAD model as shown in Fig. 11. There is satisfactory agreement for the larger RH, but significant underestimation of re-oxidation for the experiments at 24 % RH. Our model requires the reaction rate coefficient of

375   R10 to be 0.05 $M^{-1} s^{-1}$, which is a factor of 60 smaller than the value that Gonzalez et al. (2017) estimated from their model $(3 \pm 0.7 \, M^{-1} s^{-1})$. The liquid phase diffusivity of O_2 in our model is $7.1 \times 10^{-19} \, m^2 \, s^{-1}$ at 24 % RH, $1.9 \times 10^{-15} \, m^2 \, s^{-1}$ at 48 %, and $2.1 \times 10^{-14} \, m^2 \, s^{-1}$ at 65 % RH. These diffusivities of O_2 are $2 - 4$ orders of magnitude smaller than those of CO_2

determined in Dou et al. (2019). However, we need to stress that in the model, some of the iron related complex equilibrium constants and their diffusion coefficients, and the Henry's law coefficient of O_2 at different water activities are highly uncertain

380   as well, yielding to a significant uncertainty in the determination of O_2 diffusivity. For example, if the solubility of O_2 would be less than what our parameters predict now, a larger O_2 diffusivity would be consistent with our data. In addition, with the total gas flow used in our experiments, it takes about 8 min for replacing the entire EDB gas volume from N_2 to O_2, and from the response of the particle to flow condition change, we estimate an interval of about 30 min to reach full equilibration to the new gas phase conditions. Therefore, the life time of organic radicals needs to be reconsidered. In the PRAD model, we

385   do not take the radical-radical self reactions (R17) into account, which may turn out to be a significant sink for the radicals. However, it should be pointed out that the parameter set we have now is a good compromise with additional constraints from STXM/NEXAFS and CWFT experiments.

Another approximate approach to analyse the data of Fig. 11 is to use the analytical solutions for a reacto-diffusive kinetic regime. Here, O_2 taken up from the gas phase by a particle remains confined to a very thin layer below its surface compared

390   to its size provided it reacts reasonably fast with the organic components. Under these conditions there are always pairs of reaction rate and diffusion constants representing the experiments equally well (Alpert et al., 2019; Steimer et al., 2014). In the reacto-diffusive framework, with constrained reaction rate and Henry's law coefficient of O_2, the diffusion coefficient of O_2 can be estimated to be 3.6×10^{-16} and 4.4×10^{-15} m^2 s^{-1} at 48 % and 65 % RH, respectively (details are given in Appendix A4). These are both one order of magnitude less than the values from PRAD model prediction, but still consistent with each

395   other when considering all uncertainties.

3.4   HO$_2$ production measured by CWFT experiments

The CWFT experiment allows us to investigate another aspect of the photochemistry of the Fe^{III}(Cit)/CA system. According to reactions R1−R4 shown in Table 2, the HO$_2$ radical is produced upon irradiation and will partition to the gas phase. Figure 12(a) shows the RH dependence of HO$_2$ production, P_{HO_2}, from thin films in CWFT experiment. We observed that

400   P_{HO_2} increased with RH when the RH was increased from 13 % to 29 % by a factor of about 2. This may be expected since an increase from 13 % to 29 % RH leads to increasing molecular diffusion coefficients and faster chemical cycling (Lienhard et al., 2014; Song et al., 2016). However, at RH between 30 % and 60 %, P_{HO_2} decreased with RH, with a production rate at 60 % similar to the one under dry conditions. This is probably due to the decreasing concentrations of donors (e.g., Fe^{III}(Cit) and Cit$^{\cdot}$). But the decrease in concentrations with RH is too small compared the increase in diffusion coefficients with RH.

405   This means that there must be a strong sink of HO$_2$ in the condensed phase when RH increases, which has been confirmed by an increasing HO$_2$ first order loss rate as shown with black dots in Figure 12(b). When predicting P_{HO_2} with the PRAD model using a constant HO$_2$ self reaction rate of $k_5 = 8.5 \times 10^{-5}$ M^{-1} s^{-1} (Bielski et al., 1985) or a linearly increasing P_{HO_2} with RH, as in Corral Arroyo et al. (2018), the model deviates significantly from the data and does not exhibit the observed trend of decreasing P_{HO_2} for $RH > 30$ %. Both assumptions lead to a continuous increase P_{HO_2} with RH as indicated as

410   dashed and dotted blue lines in Fig. 12(a), with a decrease HO$_2$ first order loss rate as shown in Fig. 12(b), which is opposite
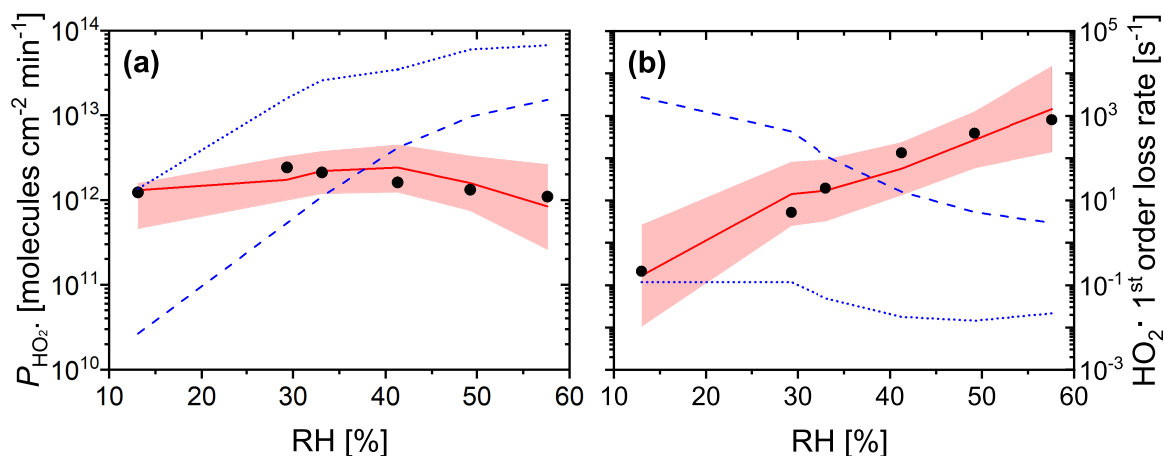
Figure 12. (a) Measured (black dots, experimental uncertainty of 3 % smaller than symbol size) and modelled (red line and shaded area) HO_2 production from continued photochemistry of $Fe^{III}(Cit)/CA$ (molar ratio of 0.07) films as a function of RH in CWFT experiments. Dotted and dashed blue lines were determined from parameterization of k_5 as a function of RH (Corral Arroyo et al., 2018) and $k_5 = 8.3 \times 10^5$ $M^{-1} s^{-1}$ in dilute aqueous solution (Bielski et al., 1985), respectively. (b) The maximum HO_2 first order loss rate determined from the result of the maximum HO_2 concentration times HO_2 self reaction rate, k_5, which was adjusted to match observations in panel (a) (black dots), or times k_5 parameterized as a function of RH for our PRAD model (Eq. (A11)) with confidence interval of 95 % (red line and shading), or times k_5 from Corral Arroyo et al. (2018) (dotted blue line), or $k_5 = 8.3 \times 10^5 M^{-1} s^{-1}$ (Bielski et al., 1985) (dashed blue line).

from our adjustment. Therefore, we argue that the effects of the increasing diffusivity and the stronger sink of HO_2 with RH compensate each other, making P_{HO_2} almost independent of RH.

3.5 Photochemical degradation under atmospheric conditions

After establishing a parameter set for the PRAD model framework which satisfactorily explains the experimental data obtained
415 with three complimentary experimental techniques over a wide parameter range, we used the model for predicting photochemical degradation of organic aerosol particles containing carboxylate complexes. For example, an aqueous organic acid particle with a dust inclusion containing iron, may exhibit a low enough pH to dissolve part of the iron of the dust inclusion and form photo-reactive iron carboxylate complexes (Dou et al., 2020). If we take the PRAD model as being representative for such a class of particles, we may estimate the degradation of the organic mass by volatilization of products to the gas phase. Figure 13
420 show examples of such PRAD model predictions: we assume that the organic mass of the particle is composed of aqueous $Fe^{III}(Cit)/CA$ with a molar ratio of the latter being 0.01. Here panel (a) illustrates size dependence and panel (b) illustrates RH dependence for particles exposed to air at 293.5 K and an actinic flux at $30°$ zenith angle (Madronich et al., 1995). After 12 hours exposure to sunlight, the organic mass of the particle (here citric acid) has been photochemically processed to CO_2 and smaller compounds of high volatility yielding a combined mass loss to the gas phase of up to 50 % depending on size and
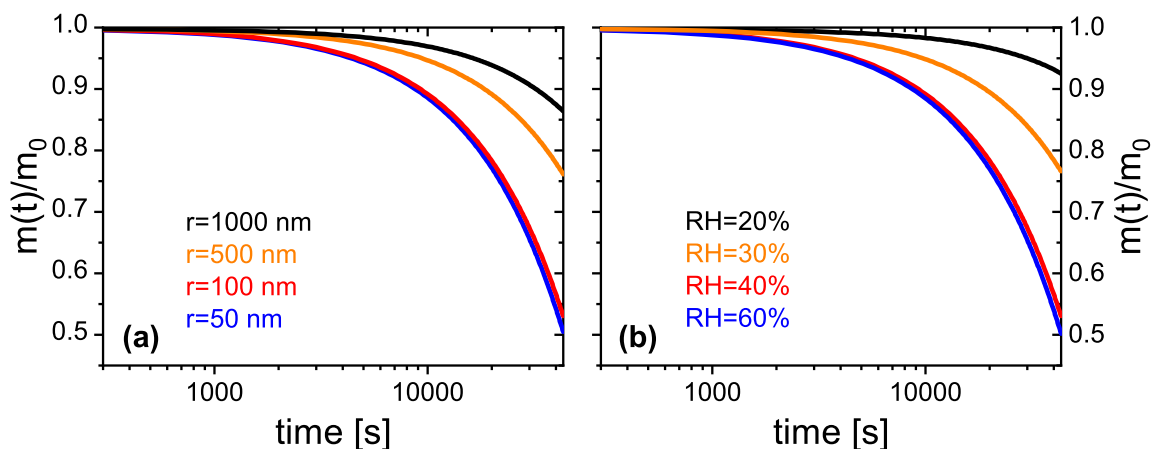
Figure 13. PRAD simulated organic mass loss of $Fe^{III}(Cit)/CA$ (molar ratio of 0.01) for (a) particles of different radii at 40% RH, and (b) particles with a radius of 100 nm at different RH. All simulations for 293.5 K and 12 h solar irradiation at 30° zenith angle (Madronich et al., 1995).

425   RH. This proves that photochemical degradation may be very significant in iron containing organic aerosol, perhaps even more important than degradation through reactions with gas phase oxidants under high particle viscosity conditions. Note, that our model does not fully capture the acceleration of degradation as discussed in Sect. 3.1. Therefore, we argue that the degradation presented in Fig. 13 represents a lower limit of the expected degradation under atmospheric conditions. Clearly, panel (a) indicates that smaller particles degrade significantly faster than larger ones. However, the size dependence is more complex

430   than a simple square law expected if reactions were purely limited by condensed phase diffusion. For particles with a radius larger than 50 nm, the time to re-partition 10 % of the mass to the gas phase depends almost linearly on size for these specific conditions. Panel (b) shows that photochemical processes are faster at higher RH corresponding to less viscous particles. The relative mass loss after 12 h irradiation between 20 % and 60 % RH is almost an order of magnitude larger for the highest RH compared to dry conditions, because of transport limitations at low RH. However, it should be noted that the relative mass

435   loss at higher humidities (between 40 % and 60 % RH) is quite similar. Here, the photochemical degradation is barely limited by condensed phase diffusivity, but by iron availability in the particle. These simulations show the potential of photochemical degradation under atmospheric conditions, a systematic study exploring the whole range of atmospheric conditions is beyond the scope to this work.

4   Conclusions

440   We used three complimentary experimental techniques to characterize the impact of reduced mobility of aerosol constituents on photochemical degradation in highly viscous particles. As an atmospherically relevant model system, we chose aque-

ous $Fe^{III}(Cit)$/CA particles. These three experimental techniques investigated specific aspects of this photochemical reaction system. In EDB experiments, we measured the mass loss relating to the continual production and loss of CO_2 and other volatile products. We observed very significant condensed phase degradation and strong acceleration of the degradation rate

445   with time. Further studies are needed to quantify all atmospheric implications, but our study suggests that photochemistry in iron containing organic aerosol will lead to a significant re-partitioning of condensed phase mass to the gas phase. We used STXM/NEXAFS to directly measure iron oxidation state in-situ with an environmental microreactor. These experiments yielded valuable information about where iron photochemical reduction and re-oxidation reactions took place, namely only very close to the surface, and it allowed to characterize to which degree iron compounds diffused inside single particles. We

450   show that O_2 uptake and diffusion into a particle is a limiting factor considering the reactions required to produce species with an oxidative potential. In addition, we found that the direct O_2 reaction with iron(II)-organic complexes does occur and generate radicals inside the particle. Flow tube experiments performed on thin $Fe^{III}(Cit)$ films showed continuous production of HO_2, revealing a radical source inside the particles driven by photochemistry.

All data were used to constrain equilibrium and kinetic parameters as well as reaction rate coefficients in a new photo-

455   chemical reaction and diffusion (PRAD) model with sufficient complexity to allow comparison with data of all experiments simultaneously. In particular, we were able to constrain the photolysis rate of Fe^{III} due to the use of various light sources with various spectral intensities, while capturing the photochemical reduction. In addition, we determined the HO_2 production rate and its first order loss rate, and the diffusivity of O_2 in aqueous $Fe^{III}(Cit)$/CA system as a function of RH and $Fe^{III}(Cit)$/CA molar ratio with a choice of O_2 related reaction rate coefficient and O_2 Henry's law coefficient.

460   As illustrated in the preceding sections, the PRAD model was able to simulate the experiments generally with satisfactory agreement. Our results and use of the PRAD model also highlight the need for future study to better constrain aspects of the iron carboxylate photochemical system. The chemical evolution of the organic species resulting from the continual photochemical oxidation was not the scope of the present study. A separate study focusing on individual OVOCs and condensed phase products is currently underway that will allow to better constrain the chemical regimes and the evolution of the oxidation state of the

465   organic fraction with time. This will also allow to assess more details of organic peroxy radical chemistry that help to explain the observed 'missing' HO_2 sink in this system. Furthermore, testing the PRAD model with different organic carboxylate ligands is desirable to broaden its applicability.

Using the PRAD model for predicting photochemical degradation for iron containing organic aerosol under atmospheric conditions let us conclude that this pathway of re-partitioning condensed phase mass to the gas phase is important and its re-

470   gional and global impact should be investigated in further modelling studies. The PRAD model may serve as a basic framework for the chemistry and transport of compounds in single particles for such studies.

Code and data availability. The data that support the findings of this study and the PRAD model code are publicly available and accessible, and from the corresponding author upon request.

Video supplement. The video supplement related to this article is available online at: https://doi.org/10.5446/47955.

Appendix A

A1 Parameterization of $D_1^j(x, T, a_{\mathrm{aw}})$

The liquid phase diffusion coefficients, $D_1^j(x, T, a_{\mathrm{w}})$, where j is an index for all species, depend on RH, T and the molar ratio, x, between $\mathrm{Fe^{III}(Cit)}$ and CA. $D_1^j(x, T, a_{\mathrm{w}})$ was scaled with the diffusion coefficient of water in $\mathrm{Fe^{III}(Cit)}$/CA aqueous system, $D_1^{\mathrm{H_2O}}(x, T, a_{\mathrm{w}})$ using a scaling factor, l_{f}^j, following

$$l_{\mathrm{f}}^j = \frac{D_1^j(x, T, a_{\mathrm{w}})}{D_1^{\mathrm{H_2O}}(x, T, a_{\mathrm{w}})}. \tag{A1}$$

$D_1^j(x, T, a_{\mathrm{w}})$ has not been previously determined for aqueous $\mathrm{Fe^{III}(Cit)}$/CA although, solution viscosity has and was found to be higher than aqueous CA solutions when $x > 0.05$ (Alpert et al., 2020), implying slower molecular transport. Lienhard et al. (2014) reported the diffusion coefficient of water in aqueous CA without iron (i.e. $x = 0$), $D_{\mathrm{CA(aq)}}^{\mathrm{H_2O}}(T, a_{\mathrm{w}})$. In order to determine $D_1^j(x, T, a_{\mathrm{w}})$ in the PRAD model for a single experiment with a fixed value of x, $D_1^{\mathrm{H_2O}}$ was scaled with $D_{\mathrm{CA(aq)}}^{\mathrm{H_2O}}(T, a_{\mathrm{w}})$ using another factor, f_{s}, following

$$D_1^{\mathrm{H_2O}}(x, T, a_{\mathrm{w}}) = D_{\mathrm{CA(aq)}}^{\mathrm{H_2O}}(T, a_{\mathrm{w}}) f_{\mathrm{s}}(x), \tag{A2}$$

where

$$\log f_{\mathrm{s}}(x) = -0.7106 e^{-\frac{1}{4x}}. \tag{A3}$$

The diffusion coefficient of CO_2 at $T = 20\,^\circ\mathrm{C}$ and $x = 0.05$, $D_{\mathrm{o}}^{\mathrm{CO_2}}$, has been independently measured by Dou et al. (2019) as a function of a_{w}. We parameterized $D_{\mathrm{o}}^{\mathrm{CO_2}}$ as

$$D_{\mathrm{o}}^{\mathrm{CO_2}} = \left(D_{\mathrm{o}}^{\mathrm{CO_2}}(a_{\mathrm{w}} = 1)\right)^{\alpha \cdot a_{\mathrm{w}}} \cdot \left(D_{\mathrm{o}}^{\mathrm{CO_2}}(a_{\mathrm{w}} = 0)\right)^{1 - \alpha \cdot a_{\mathrm{w}}}, \tag{A4}$$

where $D_{\mathrm{o}}^{\mathrm{CO_2}}(a_{\mathrm{w}} = 0) = 1.19 \times 10^{-16}\,\mathrm{m^2\,s^{-1}}$ is the diffusion coefficient of CO_2 at $T = 20\,^\circ\mathrm{C}$, $x = 0.05$ and $a_{\mathrm{w}} = 0$. The T dependent diffusion coefficient of CO_2 in water in Eq. (A4) is

$$D_{\mathrm{o}}^{\mathrm{CO_2}}(a_{\mathrm{w}} = 1) = D_0 \left(\frac{T}{T_{\mathrm{s}}} - 1\right)^m, \tag{A5}$$

where $D_0 = 1.39 \times 10^{-8}\,\mathrm{m^2\,s^{-1}}$, $T_{\mathrm{s}} = 227.0$ K and $m = 1.7094$. In the exponent terms of Eq. (A4),

$$\alpha = e^{(1 - a_{\mathrm{w}})^2 (A + B \cdot a_{\mathrm{w}})}, \tag{A6}$$

where $A = 0.2824$, and $B = -1.8086$. In order to introduce a x dependence of $D_1^{\mathrm{CO_2}}$ for various experiments reported here, f_{s} from Eq. (A3) for water was applied, following

$$D_1^{\mathrm{CO_2}}(x, T, a_{\mathrm{w}}) = D_{\mathrm{o}}^{\mathrm{CO_2}}(T, a_{\mathrm{w}}) f_{\mathrm{s}}(x). \tag{A7}$$

For all other species (excluding H_2O and CO_2), $D_1^j(x, T, a_{\mathrm{w}})$ was determined using Eq. (A1) with

$$\log l_{\mathrm{f}}^j = -0.7710 M_j^{\frac{1}{3}} - 1.4732, \tag{A8}$$
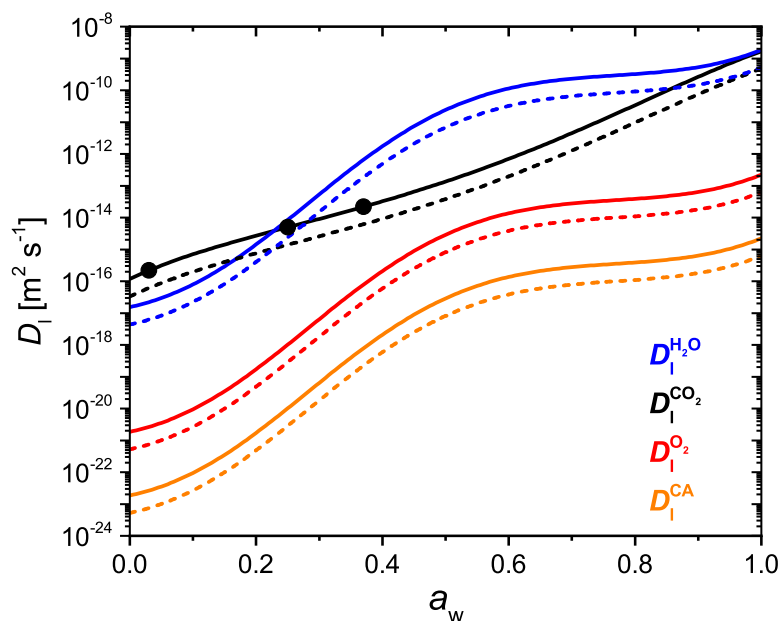
Figure A1. Parameterized liquid phase diffusion coefficients of H_2O (blue), CO_2 (black), O_2 (red), and CA (orange) as a function of water activity at $Fe^{III}(Cit)$/CA molar ratio of 0.05 (solid lines) and 1.0 (dashed lines). Three black dots are measured CO_2 diffusivity in $Fe^{III}(Cit)$/CA particle with a molar ratio of 0.05 (Dou et al., 2019). The temperature is all at 293.5 K.

where, M_j, is molar mass. Diffusion coefficients of H_2O, CO_2, O_2, and CA as a function of a_w at $x = 0.05$ and 1.0 are plotted in Fig. A1. Generally, $D_l^j(x, T, a_w)$ always decreases when RH or T is lowered. $D_l^j(x, T, a_w)$ decreases when x increases beyond 0.05, but remains relatively constant otherwise. One caveat to using Eqs. (A1)−(A8) to calculate D_l^j is that mass loss will ultimately lead to an increase in x, however, the PRAD model keeps D_l^j fixed throughout the course of a model run. Since we observed increasing mass loss rates over time, any decrease in D_l^j leading to slower chemical cycling due to increasing x was likely a minor effect. Moreover, the product distribution and any effect on diffusion coefficients was unknown, and so further time resolved adjustments to D_l^j were not considered. We suggest future studies investigate how molecular transport changes over the photochemical lifetime of iron-carboxylate complexes.

A2 Parameterization of D_g^j

The gas phase diffusivity of each species j, D_g^j, was approximated via its molar mass (M_j) compared to that of water (M_{H_2O}),

$$D_g^j = D_g^{H_2O} \sqrt{\frac{M_{H_2O}}{M_j}}, \tag{A9}$$

with

$$D_{\mathrm{g}}^{\mathrm{H_2O}} = 0.211 \left(\frac{T}{T_0}\right)^{1.94} \left(\frac{p_0}{p}\right), \qquad \text{(A10)}$$

where $T_0 = 273.15$ K, $p_0 = 1013.25$ mb, and $D_{\mathrm{g}}^{\mathrm{H_2O}}$ is in cm^2 s^{-1} (Pruppacher and Klett, 2010).

A3 Parameterization of k_5

Based on the measurement of HO$_2$ production as a function of RH using CWFT experiments, the HO$_2$ self reaction rate (R5 in Table 2), k_5, was adjusted so the PRAD model would exactly reproduce the data. We parameterized k_5 as a third degree polynomial function of RH (%):

$$\log k_5 = -2.854 \times 10^{-5} RH^3 + 0.0024 RH^2 + 0.1087 RH - 0.05018, \qquad \text{(A11)}$$

as shown in Fig. A2.
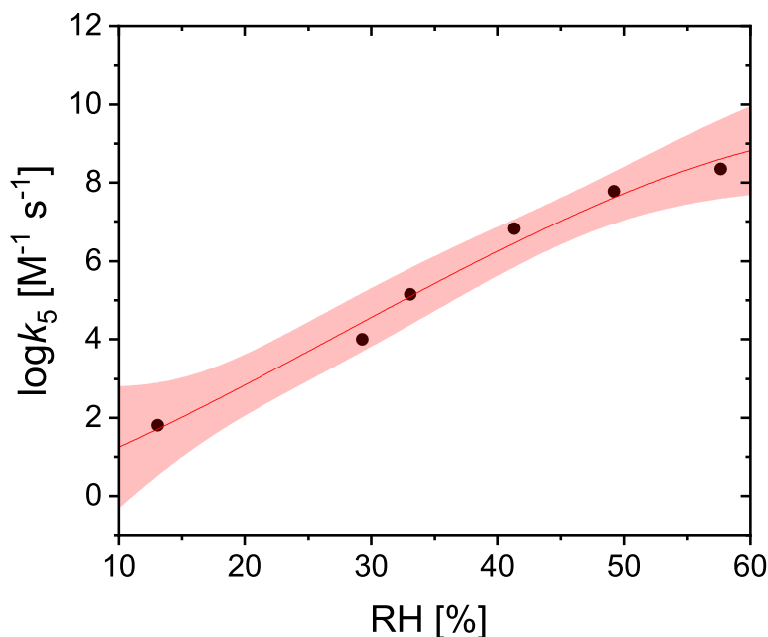
Figure A2. Adjusted values of HO$_2$ self reaction rate used in the PRAD model to exactly reproduce measured $P_{\mathrm{HO_2}}$ for CWFT experiments are shown as black dots. The red line and shading is the new parameterization (Eq. (A11)) and confidence intervals at 95 % for the HO$_2$ self reaction rate as a function of RH.

A4 β estimated by a reacto-diffusive framework

It is well known that multi-phase reactions can follow a reacto-diffusive kinetic regime (Alpert et al., 2019; Steimer et al.,
525   2014). For reacto-diffusive limitations as observed in Fig. 11, the Fe^{III} fraction as a function of time was calculated as

$$\beta(t) = 1 - (1 - Kt)^2, \tag{A12}$$

with the assumption that $\beta_0 = 0$, i.e. there was no Fe^{III} at $t = 0$.

$$K = \frac{3(H_{O_2}\sqrt{D_1^{O_2}})p_{O_2}\sqrt{k_{O_2}}}{\sqrt{[Fe_{tot}]}d_p}, \tag{A13}$$

where H_{O_2} and $D_1^{O_2}$ are Henry's law coefficient and diffusion coefficient for O_2 in the $Fe^{III}(Cit)$/CA matrix, p_{O_2} is the
530   pressure of O_2, k_{O_2} is the total reaction rate of O_2, and d_p is diameter of the single particle. $\beta = \frac{1}{e}$ when

$$t_{\frac{1}{e}} = \frac{1 - \sqrt{1 - \frac{1}{e}}}{K} = \frac{\left(1 - \sqrt{1 - \frac{1}{e}}\right)\sqrt{[Fe_{tot}]}d_p}{3(H_{O_2}\sqrt{D_1^{O_2}})p_{O_2}\sqrt{k_{O_2}}}. \tag{A14}$$

In a typical EDB experiment, $d_p = 20\ \mu m$, $H_{O_2} = 3.5 \times 10^{-2}\ M\,atm^{-1}$, $p_{O_2} = 8 \times 10^4\ Pa = 0.789\ atm$, and $k_{O_2} = 0.05$
$M^{-1}\,s^{-1}$. $[Fe_{tot}]$ is 0.3192, 0.2763, and 0.2345 M at 24 %, 48 %, and 65 % RH, respectively. From EDB data points in Fig. 11,
we estimated that $\frac{1}{e}$ of Fe^{III} can be fully recovered after around 1.7 h at 48 % RH and 0.45 h at 65 % RH. Thus the diffusion
535   coefficient of O_2 can be estimated to be 3.6×10^{-16} and $4.4 \times 10^{-15}\ m^2\,s^{-1}$ at 48 % and 65 % RH, respectively, which are both
one order of magnitude less than the values from PRAD model prediction, but still consistent with each other when considering
all uncertainties. It should be noted that in Eq. (A14), actually $H_{O_2}\sqrt{D_1^{O_2}k_{O_2}}$ is the constraint, thus any uncertainty in H_{O_2}
or k_{O_2} can change $D_1^{O_2}$.

Author contributions.   J.D. wrote the manuscript. M.A. and U.K.K. conceptualized and planned the study. J.D. conducted EDB experiments,
540   water activity measurements, and data analysis and interpretation supervised by U.K.K. P.A.A. planned and conducted STXM/NEXAFS
experiments supervised by B.W. and M.A. J.D., P.C.A., J.X., T.H., C.N.B. and K.D.H. also conducted STXM/NEXAFS experiments. B.W.,
J.R. and P.A.A. conducted STXM/NEXAFS data analysis and interpretation. P.C.A conducted CWFT experiments and data analysis and
interpretation supervised by M.A. F.S. conducted viscosity experiments and data analysis and interpretation supervised by P.A.A. B.L. wrote
and developed the PRAD model with the assistance of J.D. and P.A.A. H.H. advised on the photochemical reaction mechanisms. All co-
545   authors discussed the results and commented on the manuscript.

Competing interests.   The authors declare that they have no conflict of interest.

Acknowledgements. We thank Nir Bluvshtein for helpful discussions. We acknowledge funding by the Swiss National Science Foundation (grant no. 200021 163074/1). The PolLux end station was financed by the German Ministerium für Bildung und Forschung (BMBF) through contracts 05K16WED and 05K19WE2.

References

Abel, B., Assmann, J., Buback, M., Grimm, C., Kling, M., Schmatz, S., Schroeder, J., and Witte, T.: Ultrafast decarboxylation of carbonyloxy radicals: Influence of molecular structure, J. Phys. Chem. A, 107, 9499–9510, https://doi.org/10.1021/jp0350823, 2003.

Abida, O., Kolar, M., Jirkovsky, J., and Mailhot, G.: Degradation of 4-chlorophenol in aqueous solution photoinduced by Fe(III)–citrate complex, Photochem. Photobiol. Sci., 11, 794–802, https://doi.org/10.1039/c2pp05358f, 2012.

Abrahamson, H. B., Rezvani, A. B., and Brushmiller, J.: Photochemical and spectroscopic studies of complexes, of iron(III) with citric acid and other carboxylic acids, Inorganica Chimica Acta, 226, 117–127, https://doi.org/10.1016/0020-1693(94)04077-X, 1994.

Alpert, P. A., Corral Arroyo, P., Dou, J., Krieger, U. K., Steimer, S. S., Förster, J. D., Ditas, F., Pöhlker, C., Rossignol, S., Passananti, M., Perrier, S., George, C., Shiraiwa, M., Berkemeier, T., Watts, B., and Ammann, M.: Visualizing reaction and diffusion in xanthan gum aerosol particles exposed to ozone, Phys. Chem. Chem. Phys., 21, 20613–20627, https://doi.org/10.1039/c9cp03731d, 2019.

Alpert, P. A., Dou, J., Corral Arroyo, P., Schneider, F., Xto, J., Luo, B., Peter, T., Huthwelker, T., Borca, C. N., Henzler, K. D., Herrmann, H., Raabe, J., Watts, B., Krieger, U. K., and Ammann, M.: Anoxic aerosol particles leads to preserved radicals, in preparation for Nature, 2020.

Berkemeier, T., Steimer, S. S., Krieger, U. K., Peter, T., Pöschl, U., Ammann, M., and Shiraiwa, M.: Ozone uptake on glassy, semi-solid and liquid organic matter and the role of reactive oxygen intermediates in atmospheric aerosol chemistry, Phys. Chem. Chem. Phys., 18, 12662–12674, https://doi.org/10.1039/C6CP00634E, 2016.

Bielski, B. H. J., Cabelli, D. E., Arudi, R. L., and Ross, A. B.: Reactivity of HO_2/O_2^- radicals in aqueous solution, J. Phys. Chem. Ref. Data, 14, 1041–1100, https://doi.org/10.1063/1.555739, 1985.

Bockman, T. M., Hubig, S. M., and Kochi, J. K.: Direct observation of ultrafast decarboxylation of acyloxy radicals via photoinduced electron transfer in carboxylate ion pairs, J. Org. Chem., 62, 2210–2221, https://doi.org/10.1021/JO9617833, 1997.

Brandt, C. and van Eldik, R.: Transition metal-catalyzed oxidation of sulfur(IV) oxides. Atmospheric-relevant processes and mechanisms, Chem. Rev., 95, 119–190, https://doi.org/10.1021/cr00033a006, 1995.

Burden, R. L. and Faires, J. D.: Numerical Analysis, Brooks/Cole, Boston, MA, USA, ninth edn., 2011.

Chebbi, A. and Carlier, P.: Carboxylic acids in the troposphere, occurrence, sources, and sinks: A review, Atmos. Environ., 30, 4233–4249, https://doi.org/10.1016/1352-2310(96)00102-1, 1996.

Christensen, H. and Sehested, K.: Pulse radiolysis at high temperatures and high pressures, Radiat. Phys. Chem., 18, 723–731, https://doi.org/10.1016/0146-5724(81)90195-3, 1981.

Cieśla, P., Kocot, P., Mytych, P., and Stasicka, Z.: Homogeneous photocatalysis by transition metal complexes in the environment, J. Mol. Catal. A-Chem., 224, 17–33, https://doi.org/10.1016/j.molcata.2004.08.043, 2004.

Corral Arroyo, P., Bartels-Rausch, T., Alpert, P. A., Dumas, S., Perrier, S., George, C., and Ammann, M.: Particle-phase photosensitized radical production and aerosol aging, Environ. Sci. Technol., 52, 7680–7688, https://doi.org/10.1021/acs.est.8b00329, 2018.

Davis, E. J., Buehler, M. F., and Ward, T. L.: The double-ring electrodynamic balance for microparticle characterization, Rev. Sci. Instrum., 61, 1281–1288, https://doi.org/10.1063/1.1141227, 1990.

Deguillaume, L., Leriche, M., Desboeufs, K., Mailhot, G., George, C., and Chaumerliac, N.: Transition metals in atmospheric liquid phases: Sources, reactivity, and sensitive parameters, Chem. Rev., 105, 3388–3431, https://doi.org/10.1021/cr040649c, 2005.

585   Dou, J., Lin, P., Kuang, B. Y., and Yu, J. Z.: Reactive oxygen species production mediated by humic-like substances in atmospheric aerosols: Enhancement effects by pyridine, imidazole, and their derivatives, Environ. Sci. Technol., 49, 6457–6465, https://doi.org/10.1021/es5059378, 2015.

Dou, J., Luo, B., Peter, T., Alpert, P. A., Corral Arroyo, P., Ammann, M., and Krieger, U. K.: Carbon dioxide diffusivity in single, levitated organic aerosol particles, J. Phys. Chem. Lett., 10, 4484–4489, https://doi.org/10.1021/acs.jpclett.9b01389, 2019.

590   Dou, J., Luo, B., Peter, T., Alpert, P. A., Corral Arroyo, P., Ammann, M., and Krieger, U. K.: Photocatalytic degradation of single, levitated organic aerosol particles containing iron nanoparticles or Arizona test dust, in preparation for Geophys. Res. Lett., 2020.

Faust, B. C. and Hoigné, J.: Photolysis of Fe(III)-hydroxy complexes as sources of OH radicals in clouds, fog and rain, Atmospheric Environment. Part A. General Topics, 24, 79–89, https://doi.org/10.1016/0960-1686(90)90443-Q, 1990.

Faust, B. C. and Zepp, R. G.: Photochemistry of aqueous iron(III)-polycarboxylate complexes: roles in the chemistry of atmospheric and
595   surface waters, Environ. Sci. Technol., 27, 2517–2522, https://doi.org/10.1021/es00048a032, 1993.

Feng, W., Nansheng, D., Glebov, E. M., Pozdnyakov, I. P., Grivin, V. P., Plyusnin, V. F., and Bazhin, N. M.: Kinetics and mechanism of photolysis of the iron(III) complex with tartaric acid, Russ. Chem. Bull., 56, 900–903, https://doi.org/10.1007/s11172-007-0136-7, 2007.

Fenton, H. J. H.: LXXIII.—Oxidation of tartaric acid in presence of iron, J. Chem. Soc., Trans., 65, 899–910, https://doi.org/10.1039/CT8946500899, 1894.

600   Flechsig, U., Quitmann, C., Raabe, J., Böge, M., Fink, R., and Ade, H.: The PolLux Microspectroscopy Beam line at the Swiss Light Source, AIP Conference Proceedings, 879, 505–508, https://doi.org/10.1063/1.2436109, 2007.

Frommherz, U., Raabe, J., Watts, B., Stefani, R., Ellenberger, U., Garrett, R., Gentle, I., Nugent, K., and Wilkins, S.: Higher Order Suppressor (HOS) for the PolLux Microspectroscope Beamline at the Swiss Light Source SLS, AIP Conference Proceedings, 1234, 429–432, https://doi.org/10.1063/1.3463232, 2010.

605   Garvie, L. A., Craven, A. J., and Brydson, R.: Use of electron-energy loss near-edge fine structure in the study of minerals, American Mineralogist, 79, 411–425, 1994.

George, C., Ammann, M., D'Anna, B., Donaldson, D. J., and Nizkorodov, S. A.: Heterogeneous photochemistry in the atmosphere, Chem. Rev., 115, 4218–4258, https://doi.org/10.1021/cr500648z, 2015.

Glebov, E. M., Pozdnyakov, I. P., Grivin, V. P., Plyusnin, V. F., Zhang, X., Wu, F., and Deng, N.: Intermediates in photochemistry of Fe(III)
610   complexes with carboxylic acids in aqueous solutions, Photochem. Photobiol. Sci., 10, 425–430, https://doi.org/10.1039/C0PP00151A, 2011.

Gonzalez, D. H., Cala, C. K., Peng, Q., and Paulson, S. E.: HULIS enhancement of hydroxyl radical formation from Fe(II): kinetics of fulvic acid-Fe(II) complexes in the presence of lung antioxidants, Environ. Sci. Technol., 51, 7676–7685, https://doi.org/10.1021/acs.est.7b01299, 2017.

615   González Palacios, L., Corral Arroyo, P., Aregahegn, K. Z., Steimer, S. S., Bartels-Rausch, T., Nozière, B., George, C., Ammann, M., and Volkamer, R.: Heterogeneous photochemistry of imidazole-2-carboxaldehyde: HO2 radical formation and aerosol growth, Atmos. Chem. Phys., 16, 11 823–11 836, https://doi.org/10.5194/acp-16-11823-2016, 2016.

Hilborn, J. W. and Pincock, J. A.: Rates of decarboxylation of acyloxy radicals formed in the photocleavage of substituted 1-naphthylmethyl alkanoates, J. Am. Chem. Soc., 113, 2683–2686, https://doi.org/10.1021/ja00007a049, 1991.

620   Hofmann, H., Hoffmann, P., and Lieser, K. H.: Transition metals in atmospheric aqueous samples, analytical determination and speciation, Fresenius J. Anal. Chem., 340, 591–597, https://doi.org/10.1007/BF00322435, 1991.

Hug, S. J., Canonica, L., Wegelin, M., Gechter, D., and von Gunten, U.: Solar oxidation and removal of arsenic at circumneutral pH in iron containing waters, Environ. Sci. Technol., 35, 2114–2121, https://doi.org/10.1021/es001551s, 2001.

Huthwelker, T., Zelenay, V., Birrer, M., Krepelova, A., Raabe, J., Tzvetkov, G., Vernooij, M. G., and Ammann, M.: An in situ cell to study phase transitions in individual aerosol particles on a substrate using scanning transmission x-ray microspectroscopy, Rev. Sci. Instrum., 81, 113 706, https://doi.org/10.1063/1.3494604, 2010.

Kahnt, A., Iinuma, Y., Blockhuys, F., Mutzel, A., Vermeylen, R., Kleindienst, T. E., Jaoui, M., Offenberg, J. H., Lewandowski, M., Böge, O., Herrmann, H., Maenhaut, W., and Claeys, M.: 2-Hydroxyterpenylic acid: An oxygenated marker compound for α-pinene secondary organic aerosol in ambient fine aerosol, Environ. Sci. Technol., 48, 4901–4908, https://doi.org/10.1021/es500377d, 2014.

Kawamura, K., Ng, L. L., and Kaplan, I. R.: Determination of organic acids (C_1–C_{10}) in the atmosphere, motor exhausts, and engine oils, Environ. Sci. Technol., 19, 1082–1086, https://doi.org/10.1021/es00141a010, 1985.

Kieber, R. J., Hardison, D. R., Whitehead, R. F., and Willey, J. D.: Photochemical production of Fe(II) in rainwater, Environ. Sci. Technol., 37, 4610–4616, https://doi.org/10.1021/es030345s, 2003.

Kieber, R. J., Skrabal, S. A., Smith, B. J., and Willey, J. D.: Organic complexation of Fe(II) and its impact on the redox cycling of iron in rain, Environ. Sci. Technol., 39, 1576–1583, https://doi.org/10.1021/es040439h, 2005.

Koop, T., Bookhold, J., Shiraiwa, M., and Pöschl, U.: Glass transition and phase state of organic compounds: dependency on molecular properties and implications for secondary organic aerosols in the atmosphere, Phys. Chem. Chem. Phys., 13, 19 238–19 255, https://doi.org/10.1039/c1cp22617g, 2011.

Lienhard, D. M., Bones, D. L., Zuend, A., Krieger, U. K., Reid, J. P., and Peter, T.: Measurements of thermodynamic and optical properties of selected aqueous organic and organic-inorganic mixtures of atmospheric relevance, J. Phys. Chem. A, 116, 9954–9968, https://doi.org/10.1021/jp3055872, 2012.

Lienhard, D. M., Huisman, A. J., Bones, D. L., Te, Y.-F., Luo, B. P., Krieger, U. K., and Reid, J. P.: Retrieving the translational diffusion coefficient of water from experiments on single levitated aerosol droplets, Phys. Chem. Chem. Phys., 16, 16 677–16 683, https://doi.org/10.1039/C4CP01939C, 2014.

Madronich, S., McKenzie, R. L., Caldwell, M., and Björn, L. O.: Changes in ultraviolet-radiation reaching the earths surface, 24, 143–152, http://lup.lub.lu.se/record/134508, 1995.

Martell, A. E. and Smith, R. M.: Critical stability constants, vol. 5, Springer US, Boston, MA, USA, 1982.

Moffet, R. C., Furutani, H., Rödel, T. C., Henn, T. R., Sprau, P. O., Laskin, A., Uematsu, M., and Gilles, M. K.: Iron speciation and mixing in single aerosol particles from the Asian continental outflow, J. Geophys. Res., 117, D07 204, https://doi.org/10.1029/2011JD016746, 2012.

Okochi, H. and Brimblecombe, P.: Potential trace metal–organic complexation in the atmosphere, The Scientific World JOURNAL, 2, 767–786, https://doi.org/10.1100/tsw.2002.132, 2002.

Pozdnyakov, I. P., Kel, O. V., Plyusnin, V. F., Grivin, V. P., and Bazhin, N. M.: New insight into photochemistry of ferrioxalate, J. Phys. Chem. A, 112, 8316–8322, https://doi.org/10.1021/jp8040583, 2008.

Pozdnyakov, I. P., Glebov, E. M., Plyusnin, V. F., Grivin, V. P., Bunduki, E., Goryacheva, N. V., Gladki, V., and Duka, G. G.: Photochemistry of Fe(III) complex with glyoxalic acid in aqueous solution, High Energy Chemistry, 43, 406–409, https://doi.org/10.1134/S0018143909050129, 2009.

Pozdnyakov, I. P., Kolomeets, A. V., Plyusnin, V. F., Melnikov, A. A., Kompanets, V. O., Chekalin, S. V., Tkachenko, N., and Lemmetyinen, H.: Photophysics of Fe(III)–tartrate and Fe(III)–citrate complexes in aqueous solutions, Chemical Physics Letters, 530, 45–48, https://doi.org/10.1016/j.cplett.2012.01.051, 2012.

660   Pruppacher, H. and Klett, J.: Microstructure of atmospheric clouds and precipitation, in: Microphysics of Clouds and Precipitation, vol. 18, pp. 10–73, Springer Netherlands, Dordrecht, https://doi.org/10.1007/978-0-306-48100-0_2, 2010.

Raabe, J., Tzvetkov, G., Flechsig, U., Böge, M., Jaggi, A., Sarafimov, B., Vernooij, M. G., Huthwelker, T., Ade, H., Kilcoyne, D., Tyliszczak, T., Fink, R. H., and Quitmann, C.: PolLux: A new facility for soft x-ray spectromicroscopy at the swiss light source, Rev. Sci. Instrum., 79, 113 704, https://doi.org/10.1063/1.3021472, 2008.

665   Rush, J. D. and Bielski, B. H. J.: Pulse radiolytic studies of the reaction of HO_2/O_2^- with Fe(II)/Fe(III) ions. The reactivity of HO_2/O_2^- with ferric ions and its implication on the occurrence of the Haber-Weiss reaction, J. Phys. Chem., 89, 5062–5066, https://doi.org/10.1021/j100269a035, 1985.

Sander, R.: Compilation of Henry's law constants (version 4.0) for water as solvent, Atmos. Chem. Phys., 15, 4399–4981, https://doi.org/10.5194/acp-15-4399-2015, 2015.

670   Shiraiwa, M. and Seinfeld, J. H.: Equilibration timescale of atmospheric secondary organic aerosol partitioning, Geophys. Res. Lett., 39, L24 801, https://doi.org/10.1029/2012GL054008, 2012.

Shiraiwa, M., Ammann, M., Koop, T., and Poschl, U.: Gas uptake and chemical aging of semisolid organic aerosol particles, Proc. Natl. Acad. Sci., 108, 11 003–11 008, https://doi.org/10.1073/pnas.1103045108, 2011.

Smith, R. M. and Martell, A. E.: Critical Stability Constants, vol. 4, Springer US, Boston, MA, USA, https://doi.org/10.1007/978-1-4757-
675   5506-0, 1976.

Song, Y. C., Haddrell, A. E., Bzdek, B. R., Reid, J. P., Bannan, T., Topping, D. O., Percival, C., and Cai, C.: Measurements and predictions of binary component aerosol particle viscosity, J. Phys. Chem. A, 120, 8123–8137, https://doi.org/10.1021/acs.jpca.6b07835, 2016.

Steimer, S. S., Lampimäki, M., Coz, E., Grzinic, G., and Ammann, M.: The influence of physical state on shikimic acid ozonolysis: a case for in situ microspectroscopy, Atmos. Chem. Phys., 14, 10 761–10 772, https://doi.org/10.5194/acp-14-10761-2014, 2014.

680   Steimer, S. S., Berkemeier, T., Gilgen, A., Krieger, U. K., Peter, T., Shiraiwa, M., and Ammann, M.: Shikimic acid ozonolysis kinetics of the transition from liquid aqueous solution to highly viscous glass, Phys. Chem. Chem. Phys., 17, 31 101–31 109, https://doi.org/10.1039/C5CP04544D, 2015a.

Steimer, S. S., Krieger, U. K., Te, Y. F., Lienhard, D. M., Huisman, A. J., Luo, B. P., Ammann, M., and Peter, T.: Electrodynamic balance measurements of thermodynamic, kinetic, and optical aerosol properties inaccessible to bulk methods, Atmos. Meas. Tech., 8, 2397–2408,
685   https://doi.org/10.5194/amt-8-2397-2015, 2015b.

von Sonntag, C. and Schuchmann, H.-P.: Aufklärung von Peroxyl-Radikalreaktionen in wäßriger Lösung mit strahlenchemischen Techniken, Angew. Chem., 103, 1255–1279, https://doi.org/10.1002/ange.19911031006, 1991.

Walling, C.: Fenton's reagent revisited, Acc. Chem. Res., 8, 125–131, https://doi.org/10.1021/ar50088a003, 1975.

Wang, Z., Chen, C., Ma, W., and Zhao, J.: Photochemical coupling of iron redox reactions and transformation of low-molecular-weight
690   organic matter, J. Phys. Chem. Lett., 3, 2044–2051, https://doi.org/10.1021/jz3005333, 2012.

Weller, C., Horn, S., and Herrmann, H.: Photolysis of Fe(III) carboxylato complexes: Fe(II) quantum yields and reaction mechanisms, J. Photochem. Photobiol. A Chem., 268, 24–36, https://doi.org/10.1016/j.jphotochem.2013.06.022, 2013.

Weller, C., Tilgner, A., Bräuer, P., and Herrmann, H.: Modeling the impact of iron-carboxylate photochemistry on radical budget and carboxylate degradation in cloud droplets and particles, Environ. Sci. Technol., 48, 5652–5659, https://doi.org/10.1021/es4056643, 2014.

695   Weschler, C. J., Mandich, M. L., and Graedel, T. E.: Speciation, photosensitivity, and reactions of transition metal ions in atmospheric droplets, J. Geophys. Res., 91, 5189, https://doi.org/10.1029/JD091iD04p05189, 1986.

Willey, J. D., Kieber, R. J., Williams, K. H., Crozier, J. S., Skrabal, S. A., and Avery, G. B.: Temporal variability of iron speciation in coastal rainwater, J. Atmos. Chem., 37, 185–205, https://doi.org/10.1023/A:1006421624865, 2000.

Zardini, A. A., Krieger, U. K., and Marcolli, C.: White light Mie resonance spectroscopy used to measure very low vapor pressures of substances in aqueous solution aerosol particles, Optics Express, 14, 6951–6962, https://doi.org/10.1364/OE.14.006951, 2006.

Zhang, X., Gong, Y., Wu, F., Deng, N., Pozdnyakov, I. P., Glebov, E. M., Grivin, V. P., Plyusnin, V. F., and Bazhinb, N. M.: Photochemistry of the iron(III) complex with pyruvic acid in aqueous solutions, Russ. Chem. Bull, 58, 1828–1836, https://doi.org/10.1007/s11172-009-0249-2, 2009.

700